Stony Brook University

OFFICIAL COPY

The official electronic file of this thesis or dissertation is maintained by the University Libraries on behalf of The Graduate School at Stony Brook University.

© All Rights Reserved by Author.

Compressible Multi Phase and Multi Species Flow Closure Model and Turbulent Analysis for Rayleigh-Taylor Instability

A Dissertation Presented

by

Hyunsun Lee

to

The Graduate School in Partial Fulfillment of the Requirements for the

Degree of

Doctor of Philosophy

in

Applied Mathematics and Statistics

(Computational Applied Mathematics)

Stony Brook University

August 2007

Stony Brook University

The Graduate School

Hyunsun Lee

We, the dissertation committee for the above candidate for the Doctor of Philosophy degree, hereby recommend acceptance of this dissertation.

James Glimm
Professor of Applied Mathematics and Statistics
Dissertation Advisor

Xiaolin Li
Professor of Applied Mathematics and Statistics
Chairperson of Defense

Brent Lindquist
Professor of Applied Mathematics and Statistics

Roman Samulyak
Brookhaven National Laboratory
Outside Member

This dissertation is accepted by the Graduate School.

Lawrence Martin
Dean of the Graduate School

Abstract of the Dissertation

Compressible Multi Phase and Multi Species Flow Closure Model and Turbulent Analysis for Rayleigh-Taylor Instability

by

Hyunsun Lee

Doctor of Philosophy

in

Applied Mathematics and Statistics

(Computational Applied Mathematics)

Stony Brook University

2007

This thesis discusses the 3D Rayleigh-Taylor instability, which occurs when a dense, heavy fluid is accelerated by a light fluid, yielding initially well defined bubbles and spikes of light and heavy fluid, each penetrating into the other fluid, followed by the development of a layer consisting of a complex mixing flow regime.

We introduce primitive governing equations of the fluid mixing and average them to propose a new simple closure model for compressible multi phase and multi species flow with surface tension and transport terms. The closure model is validated against 'FronTier' simulations based on front tracking method. The simulation data is also validated separately against laboratorial experiments. We start with microscopic equations for conservation of mass, momentum, and energy. By multiplying the microscopic equations by a phase indicator function and averaging, the averaged equations for each phase are obtained. For the averaging, we use the ensemble average based on the method and assumptions proposed by D. A. Drew and S. L. Passman. The averaging process usually results in undefined averages of nonlinear functions of the primitive variables, which have to be remodeled to close the system of equations. We define three interfacial quantities and propose a general closure model for these quantities, which satisfies all the conservation and boundary conditions. In our closure model, most of parameters are irrelevant and can be set to 1. We prove that the error of our model is around 10% average over all our simulations by comparing it with the exact expression of simulations of the two vluid microscopic equations.

As a further examination of the two fluid micdroscopic simulation, mesh refinement and insertion of a calibrated Smagorinsky subgrid model are applied. First we perform spectral analysis to compare our result with classical turbulence study, especially the Kolmogorov power law decay rate. Another comparison is done by averaging the molecular mixing parameter over a certain number of grid cells, yielding a conventionally expected value. Averaging of data over volumes with $4\triangle x$ to $8\triangle x$ side length gives the expected value for ideal and surface tension cases. The miscible simulations yield this result without any averaging. The typical upturns in spectra of velocity, density and kinetic energy at large wavenumbers give a clue to assess the necessity or desirability of subgrid model. We adopt one of the simplest subgrid model, Smagorinsky type. But the magnitude of subgrid model is expected to be small, in view of the small size of the upturn.

Key Words: Rayleigh-Taylor instability, closure, turbulence, Kolmogorov power, Smagorinsky subgrid.

Table of Contents

List of Figures

List of Tables

Acknowledgements

I would like to express the deepest appreciation to my adviser, Professor Glimm, who has the attitude and the substance of a great researcher and mentor. He always showed me his enthusiasm to the work, which I tried to model in doing my part of work. He conveyed not only his broad knowledge on the research but also the advanced methodology. In addition to these, I thank him for giving me the wisdom on coworking with others, which, I believe, is the most important part in research. Without his guidance and persistent help this dissertation would not have been possible. I also thank my committee members for their patience and consideration.

I thank Thora and Susan who were another advisers in my life here. They always gave me good advice and extra strength to overcome all the hard time in my real life and my research. I cannot forget Sergei's effort to take care of me, thank him for all his support. Thank Yeona for her deep understanding me. Thank all my coworkers. I will miss you and our group meetings. Thank my soulmate, Dayoung, for encouraging me all the time. Thank my forever best friends, Yumi and Yeojung, in Korea.

Above all these people, the reason I can be standing here is that my parents are always supporting me. I really appreciate their pure love and trust for me. I am very proud of myself that I am brave and honest enough to say something is wrong when it is wrong rather than hide it in any circumstance, which my parents thought me during my life with them. I also thank my brother and all my relatives.

I am happy and lucky to have you all.

Chapter 1

Front Tracking

In this chapter we briefly introduce a package, 'FronTier', for front tracking. This package is used for simulations of interfaces and provide the main source of data analysis in later chapters 3 and 4. This chapter is only for the purpose of explaining of how the interface is tracked, initially set and propagated. A more detailed description of this package can be found in [12].

1.1 Locally Grid Based Tracking

Locally grid based method of front tracking results from a merging of two different methods, the grid free method and the grid based method. In the grid free tracking, the interface does not have any relation to a finite difference grid. It is freely propagating through a rectangular grid. This method is very accurate but not robust with regard to a topological bifurcation. In grid based tracking, the front is regularized or reconstructed based on a finite grid at each time step. After propagation, the points which intersect with all grid cell edges are found. We here assume that there is no more than one intersection point on each grid cell edge; enforcement of this criteria is the key step in resolving topological ambiguities. Then the interface is reconstructed simply by linearly connecting these crossing points. This grid based tracking is not very accurate but very robust.

Locally grid based tracking method takes advantage of these two methods, depending on the more accurate grid free tracking in the region without any bifurcation, and the more robust grid based tracking in the region with bifurcation by constructing a small box around it. Grid based propagation is performed in the box and the propagated surface is reconnected to the grid free surface triangulation around the box. The result of this locally grid based tracking method is plausible since it preserves the accuracy of grid free tracking and the robustness of grid based tracking. Figure 1.1 clearly shows the advantage of using the locally grid based method for tracking the interface. In this sense it is comparable to the hybrid particle level set method which combines Eulerian front capturing and Lagrangian front tracking methods.

1.2 Static Interface

The interface can be described as a discrete topological manifold which is a group of linked points. The interface consists of points and curves in $2D$, points, curves and surfaces in $3D$. Curves and surfaces have pointers to the objects which organize the boundary and the object it bounds. The start and end points of a curve are called nodes. The curves and surfaces are composed of linear segments, and each linear segment has pointers to connect it to its neighbors. The interface objects are constructed in each rectangular block by detecting crossing points and connecting them with the linear segments, and are linked to neighbors. After that, a redistribution of the interface is needed to optimize the bonds in $2D$ and triangles in $3D$. To optimize points on curves in $2D$, the total length of the curve is measured and divided by the total number of bonds so that each new bond has the same length. In 3D the area ratio of the triangles are calculated and by deletion and re-triangulation

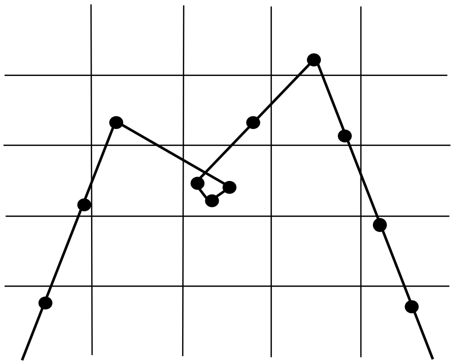

Grid Free Interface

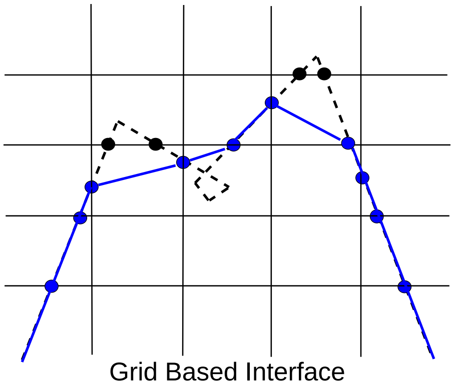

Grid Based Interface

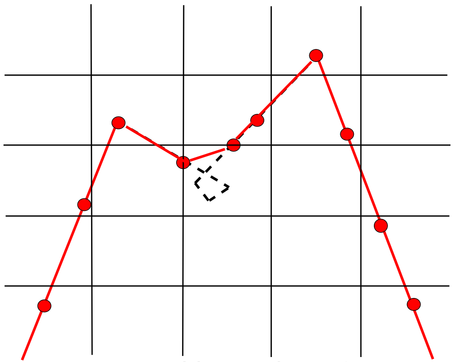

Locally Grid Based Interface

Figure 1.1: Grid free interface (top), grid based (middle) and locally grid based (bottom)

all the new triangles are controlled to satisfy our criterion.

1.3 Interface Propagation

Interface propagation is achieved by point propagation. There are two different types of point propagation. One type of propagation is based on a velocity field which is a function of position and time. The moving front is advanced by solving a ordinary equation

$$\frac{dx}{dt} = v(x,t) \ , \tag{1.1}$$

for example, with a first order Euler or a fourth order Runge-Kutta method. The second type of interface propagation is hyper surface propagation. In this case the velocity depends on not only position and time but also interface normal and curvature. As one point propagates, its neighbors move so that the normal and curvature change.

Chapter 2

Rayleigh-Taylor Instability and Simulations

In this chapter we introduce the basic terminology of the Rayleigh-Taylor Instability. Our simulation settings are also presented.

2.1 Initial Conditions

The computational domain of our simulations is $2 \times 2 \times 8$ in the x_1, x_2 and x_3 directions with a grid size $128 \times 128 \times 512$ as the finest resolution. The interface is initially perturbed by a random combination of Fourier modes. For the mass diffusion and surface tension simulations, the mode numbers ranged from 8 to 16, generating an initial averaged number of modes is 12×12 bubbles which means there are 12 bubbles in each direction. For the ideal simulation, the mode numbers ranged from 4 to 8. The initial interface position is given as a Fourier series

$$x_3(x_1, x_2) = x_{3,0} + \sum_{n_1, n_2} \left(a_{n_1,n_2} \sin(n_1 x_1 + n_2 x_2) + b_{n_1,n_2} \cos(n_1 x_1 + n_2 x_2) \right), \qquad (2.1)$$

where $x_{3,0}$ is the unperturbed interface position, which is initially set at the middle of the domain height, $x_{3,0} = 4$. The coefficients a_{n_1,n_2} and b_{n_1,n_2} are chosen as Gaussian random variables, with mean of 0 and standard deviation of 0.001. Periodic boundaries are imposed on the x_1, x_2 sides of the domain and Neumann boundaries are imposed on the top and the bottom of the domain. The initial flow field is unperturbed, with a zero velocity, constant temperature fields and pressure and density in each of the fluids specified by hydrostatic isothermal equilibrium.

The light fluid is initially placed above the heavy fluid. The density ratio is 3 : 1 so that the Atwood number $A = (\rho_2 - \rho_1)/(\rho_2 + \rho_1)$ at the initial interface (at the initial time $t = 0$) is $A = 0.5$. The simulations are conducted in the frame of an experimental container subject to a strong steady downwards acceleration, effectively reversing the direction of gravity, which thus points upward.

To describe the compressibility of our simulations we use the dimensionless constant

$$M^2 = \lambda g / c_h^2 \ , \tag{2.2}$$

where c_h is the sound speed in the heavy fluid. In the three cases of simulations analyzed here, the compressibility is $M^2 = 0.008$. The small value of M^2 brings a good approximation to nearly incompressible laboratory experiments, in the sense that the density variation throughout the heavy and light fluids due to gravitational stratification is small in both of the experiments and the simulations.

2.2 Rayleigh-Taylor Instability Simulations

Rayleigh-Taylor (RT) instability, named after Lord Rayleigh and G.I. Taylor, occurs when a dense, heavy fluid is accelerated by a light fluid. Bubbles of light fluid and spikes of heavy fluid penetrate into the other, resulting in the development of a complex mixing layer. We are dealing with three different cases, ideal, immiscible with surface tension and miscible with mass diffusion. For instance, we can imagine that water is placed on top of oil separated by a very thin layer, and suddenly the layer disappears, making some initial perturbation. These two fluids start to mix for density difference. Or when we put creme in coffee, they mix in a molecular level. These examples show surface tension and mass diffusion cases, respectively. Ideal case, however, cannot occur in the real world so that it is not possible to compare such simulations to experiments.

In our simulations, the ideal simulation [15] has no surface tension, no mass diffusion, no physical viscosity and no thermal conductivity. The surface tension simulation [15] has a dimensionless surface tension $\tilde{\sigma}$ equal to the experimental value [28, 30]. The dimensionless surface tension is defined as

$$\tilde{\sigma} = \sigma/(\lambda^2 \Delta\rho g) \ . \tag{2.3}$$

where σ is the corresponding dimensional surface tension, and λ is an initial wave length characterizing the initial perturbations. ρ and g are density and gravity. In our simulation, λ is $2/12 = 0.167$ and the constant gravity is 0.14. The third simulation with physical mass diffusion [22, 23] models the Banerjee-Andrews air-helium Rayleigh-Taylor experiments [1]. The mass diffusivity is dimensionalized using an initial wave length scale set from observation of the flow, and with this setting, the dimensionless simulation mass diffusivity is identical to the dimensionless experimental value, and expressed as

$$\tilde{\nu} = \nu/(\lambda\sqrt{Ag\lambda}) \, . \tag{2.4}$$

This simulation yields $\alpha = 0.069$ in agreement with experiment.

We compare simulations and experiments in terms of the growth rate of the mixing zone. To do this we prefer the growth rate of the bubble side of the mixing layer rather than that of the spike side as the numerical results are more accurate in this case. We define the bubble growth rate by the dimensionless constant α in the

Experiment Simulation	Comment	α	$\tilde{\sigma}$
Read-Youngs	Immiscible [28] # 29	0.073	5.7E-3
Read-Youngs	Immiscible [28] # 35	0.066	4.6E-3
Smeeton-Youngs	Immiscible [30] #104	0.066	8.8E-3
Smeeton-Youngs	Immiscible [30] #105	0.072	7.3E-3
Smeeton-Youngs	Immiscible [30] #114	0.060	7.8E-3
Centroid	± deviation	0.066 ± 0.006	
Average	± 2 STD	0.068 ± 0.005	
FronTier (high resolution)	Immiscible	0.068	7E-3
FronTier (low resolution)	Immiscible	0.056	7E-3
TVD	Ideal Untracked [14]	0.035-0.034	0.0
FronTier	Ideal Tracked	0.09-0.078	0.0

Table 2.1: Mixing rates compared: FronTier simulation compared to immiscible experiments and contrasted to untracked (TVD) and ideal fluid FronTier simulations.

equation

$$h_b = \alpha A g t^2 \ . \tag{2.5}$$

The bubble of the light fluid penetrates into the heavy fluid by height, h_b, relative to the initial interface which is $x_3 = 4$. Table 2.1 shows the values of $\alpha = \alpha_b$ and the dimensionless surface tension $\tilde{\sigma}$ in different experiments and simulations.

Chapter 3

Closure Model

In this chapter we propose a closure model for the interfacial quantity of v, p and pv. We start by introducing ensemble average and the phase indicator function to obtain the phase averaged equations. From these macroscopic equations, we directly derive the exact expressions for the three interfacial quantities. By modelling coefficients in these interfacial quantities we have our closure model. This model is compared by another models which were proposed by others.

3.1 Ensemble Average and the Phase Indicator Function

The ensemble average is the mean of a quantity which is a function of the microstate of a system. It is a central concept in statistical mechanics. Here we use the notation, $< \cdot >$, which implies the spatial average over the x_1, x_2-plane in a 3D Rayleigh-Taylor instability.

This average satisfies

$$\begin{aligned} \langle f+g\rangle &= \langle f\rangle + \langle g\rangle \ , \\ \langle\langle f\rangle g\rangle &= \langle f\rangle \langle g\rangle \ , \\ \langle c\rangle &= c \ , \\ \left\langle \frac{\partial f}{\partial t}\right\rangle &= \frac{\partial \langle f\rangle}{\partial t} \ , \\ \left\langle \frac{\partial f}{\partial x_i}\right\rangle &= \frac{\partial \langle f\rangle}{\partial x_i} \ , \end{aligned}$$

where c is constant. The first three of these are called Reynolds' rules, the fourth is Leibniz' rule and the fifth is Gauss' rule [10, 11].

We use two kinds of averaging for variables, one is the phase average and the other is the phase mass-weighted average. For a variable f, the phase average is defined as

$$f_k = \langle X_k f\rangle / \langle X_k\rangle \ , \tag{3.1}$$

and the phase mass-weighted average is defined as

$$f_k = \langle X_k \rho f\rangle / \langle X_k \rho\rangle \ , \tag{3.2}$$

where ρ is density and X_k is a phase indicator function. Here the phase indicator function is a time and position dependent function, which, literally shows if the position is in a given phase or not, and is defined as

$$X_k(\mathrm{x},\mathrm{t}) = \begin{cases} 1 & \text{if x is in phase k} \\ 0 & \text{otherwise} \end{cases}$$

This means that the indicator function is 1 when the position x is in phase k at time t and otherwise 0. This is a good definition for the ideal and immiscible cases but it is an ambiguous definition for miscible case. In this case we use the 50% concentration contour of each fluid as the interface. We introduce a substitute, relative concentration, for this definition for the miscible case in chapter 4.

The ensemble average of the indicator function X_k is denoted by $\beta_k \equiv \langle X_k \rangle$. Then $\beta_k(x_3, t)$ is the volume fraction of the horizontal layer at height x_3 that is occupied by fluid k at time t. Since each X_k is between 0 and 1, the volume fraction, which is the average of X_k values, must be also between 0 and 1. We notice here that β_k is usually continuous even though X_k is discontinuous.

Figure 3.1 shows the Rayleigh-Taylor mixing in a hexahedron $[0, 2] \times [0, 2] \times [0, 8]$ at time $t = 9.5$ and Figure 3.2 is the distribution of the two fluids. This figure shows the evolution of the bubbles of light fluid and the spikes of heavy fluid which are penetrating in the opposite fluid at the height $x_3 = 4.5$. Here the mixing zone which is defined as the region from bubble tip to spike tip (usually we use $5 \sim 95$ percent of the whole mixing zone) is $3.376 \sim 4.761$. Since we initially set the light fluid on the top and the heavy fluid on the bottom (the gravity is set going upward) the oval objects in Figure 3.2 are spikes or stems of heavy fluid surrounded by the ambient light fluid considering that the height $x_3 = 4.5$ is more on the spike side. Inside these objects the phase indicator function $X_1 = 0$ and $X_2 = 1$ while $X_1 = 1$ and $X_2 = 0$ outside the objects. The corresponding volume fraction is $\beta_1(x_3, t) = \beta_1(4.5, 9.5) = 0.862$ and $\beta_2(x_3, t) = \beta_2(4.5, 9.5) = 1 - \beta_1(4.5, 9.5) = 0.138$ at the height $x_3 = 4.5$ and the time $t = 9.5$.

The property of the phase indicator function brings us to the topological equation expressed as

$$\frac{\partial X_k}{\partial t} + v_{\text{int}} \cdot \nabla X_k = 0 \ . \tag{3.3}$$

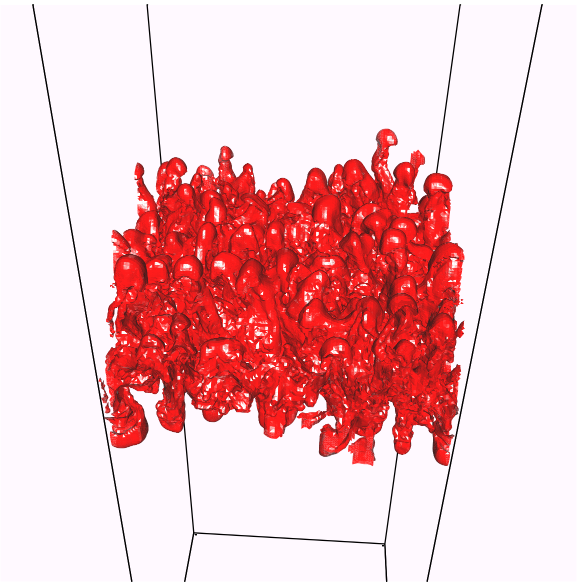

Figure 3.1: RT simulation

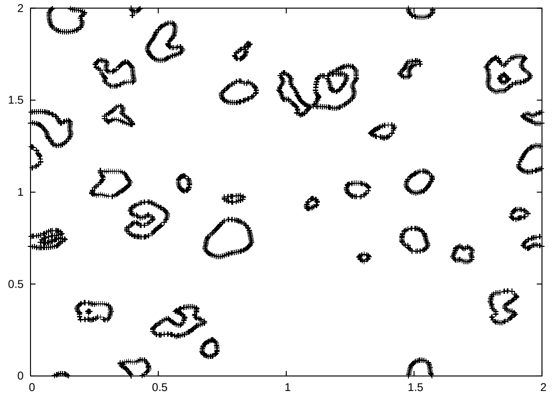

Figure 3.2: The distribution of the light fluid and the heavy fluid at the height $z = 4.5$ Inside the objects $X_1 = 0$ and $X_2 = 1$ and outside the objects $X_1 = 1$ and $X_2 = 0$.

The left side of this equation is the material derivative of X_k following the interface. On a point, not on the interface, either $X_k = 0$ or $X_k = 1$. In either case the partial derivatives vanish and satisfy the equation (3.3). When a point on the interface moves with the interface velocity then the function X_k is a jump that remains constant, which also makes the equation hold. The velocity component normal to the boundary is continuous so that $v_{\text{int}} \cdot \nabla X_k$ is well defined.

3.2 General Understanding of Closure

Consider Burger's equation,

$$U_t + UU_x = 0 \ , \tag{3.4}$$

that is,

$$U_t + \frac{1}{2}\left(U^2\right)_x = 0 \ . \tag{3.5}$$

After ensemble average for the both sides of this Burger's equation (3.5) and by using the first one of Reynolds' rules and Leibniz' rule in the ensemble average properties (3.1), the equation becomes

$$\langle U \rangle_t + \frac{1}{2}\left\langle U^2 \right\rangle_x = 0 \ . \tag{3.6}$$

We here have one equation and two unknowns $< U >$ and $< U^2 >$ which are the first and the second moments. To solve this we multiply U to the both sides of the equation (3.4) and average it again, then it becomes

$$\frac{1}{2}\left\langle U^2 \right\rangle_t + \frac{1}{3}\left\langle U^3 \right\rangle_x = 0 \ , \tag{3.7}$$

we have two equations and three unknowns. If we keep repeating this precision we always have one more unknowns than equations, since $\langle U^n \rangle \neq \langle U \rangle^n$ in general, so that the system is not solvable. Thus this is not a closed system. Thus we have to close the system by modelling $\left\langle U^(n+1) \right\rangle$ as a function of $\langle U \rangle, \langle U^2 \rangle \cdots \langle U^n \rangle$ for some positive integer n. Then we have n equations and n unknowns, and a formally solvable system of equations.

This is the basic idea for closure. In a couple of following sections we introduce the original equations which we call the primitive equations and average the phase primitive equations obtained by multiplying the phase indicator function to the primitive equations. We reformulate the nonlinear terms to gain our closure model.

3.3 The Primitive Equations

Many numerical simulations in fluid dynamics are based on the Euler or Navier-Stokes equations. We deal with multi species and multi phase flow with indices i and k, respectively. A species is a microscopic atomic or molecular unit and distinguished from phase which is the tangible state of matter such as a solid, a liquid, or vapor.

We start from the single-phase Navier-Stokes equations. The following equations are the microscopic continuity, momentum and energy equations in an inertial frame.

$$\frac{\partial \rho_i}{\partial t} + \nabla \cdot \rho_i \mathbf{v} = -\nabla \cdot \mathbf{j}_i \ , \tag{3.8}$$

$$\frac{\partial \rho \mathbf{v}}{\partial t} + \nabla \cdot \rho \mathbf{v}\mathbf{v} = \nabla \cdot \tau + \rho \mathbf{g} \ , \tag{3.9}$$

$$\frac{\partial \rho E}{\partial t} + \nabla \cdot \rho \mathbf{v} E = \nabla \cdot \tau \mathbf{v} + \rho \mathbf{v} \cdot \mathbf{g} - \nabla \cdot \sum_i h_i \mathbf{j}_i + \nabla \cdot \kappa \nabla T \ . \tag{3.10}$$

where ∇ is the gradient operator and $\nabla \cdot$ is the divergence operator. The dependent variables ρ_i, $\mathbf{v}$, $\rho = \sum_i \rho_i$, p, E, and $\mathbf{g}$ denote, respectively, the species i mass density, the velocity, total density, pressure, total energy with $E = e + \mathbf{v}^2/2$ and e the internal energy and gravity. The specific enthalpy of species i is

$$h_i = e_i + \frac{p_i}{\rho_i} \tag{3.11}$$

where p_i is the partial pressure of species i; e_i is the specific internal energy of species i. τ is the total stress. We consider Newtonian fluids for which viscosity depends only on temperature and pressure, so that the constitutive law for the Cauchy stress is of the form,

$$\tau = -p\mathbf{I} + \tau' \ , \tag{3.12}$$

where τ' is the viscous stress. Note that the rate of deformation tensor ($\mathbf{D}$) can be broken into a spherical part ($\mathring{\mathbf{D}}$) and deviatoric part ($\hat{\mathbf{D}}$).

$$\mathbf{D} = \frac{1}{2}\left[\nabla\mathbf{v} + (\nabla\mathbf{v})^T\right] = \mathring{\mathbf{D}} + \hat{\mathbf{D}} \ , \tag{3.13}$$

where $\mathring{\mathbf{D}}$ represents pure volumetric rate of deformation and is simply proportional to the sum of the diagonal element of $\mathbf{D}$,

$$\mathring{\mathbf{D}} = \frac{1}{3}\mathrm{tr}(\mathbf{D})\mathbf{I} \tag{3.14}$$

and $\hat{\mathbf{D}}$ is pure shear rate of deformation,

$$\hat{\mathbf{D}} = \mathbf{D} - \mathring{\mathbf{D}} = \mathbf{D} - \frac{1}{3}\mathrm{tr}(\mathbf{D})\mathbf{I} \ . \tag{3.15}$$

Then the viscous stress $\mathbf{T}'$ can be expressed by

$$\begin{aligned}\mathbf{T}' &= 3\mu^{bulk}\mathring{\mathbf{D}} + 2\mu^{shear}\hat{\mathbf{D}} \\ &= 2\mu^{shear}\left[\mathbf{D} - \frac{1}{3}\mathrm{tr}(\mathbf{D})\mathbf{I}\right] + \mu^{bulk}\mathrm{tr}(\mathbf{D})\mathbf{I} \qquad (3.16)\end{aligned}$$

where μ^{shear} is called the first coefficient of viscosity or shear viscosity and μ^{bulk} the bulk viscosity. Also κ is the heat conductivity and T is temperature. The total mass density is $\rho = \sum_i \rho_i$ and $\omega_i = \rho_i/\rho$ is the mass fraction of the ith species. $\mathbf{j}_i$ is the diffusion flux of the form

$$\mathbf{j}_i = -\rho \sum_k \nu_{i,k} \nabla \omega_i \ , \qquad (3.17)$$

where $\nu_{i,j}$ are binary diffusion coefficients which are subject to the constraints [2]

$$\nu_{i,i} = 0, \qquad (3.18)$$

$$\textstyle\sum_i (\nu_{i,j} - \nu_{i,k}) = 0, \ j \neq k \ . \qquad (3.19)$$

For the two species case, $\nu_{1,2} = \nu_{2,1}$. In general, the $\nu_{i,j}$, as with the other transport coefficients and the surface tension, are thermodynamic functions, and thus dependent on temperature, pressure and the concentrations $\omega_1, \omega_2, \cdots, \omega_N$. If we plug $\omega_i = \rho_i/\rho$ in the microscopic continuity equation (3.8),

$$\frac{\partial \omega_i \rho}{\partial t} + \nabla \cdot \omega_i \rho \mathbf{v} = -\nabla \cdot \mathbf{j}_i \qquad (3.20)$$

$$\omega_i\left(\frac{\partial \rho}{\partial t} + \nabla \cdot \rho \mathbf{v}\right) + \rho\left(\frac{\partial \omega_i}{\partial t} + \mathbf{v} \cdot \nabla \omega_i\right) = -\nabla \cdot \mathbf{j}_i \qquad (3.21)$$

Since the total mass is conserved,

$$\frac{\partial \rho}{\partial t} + \nabla \cdot \rho \mathbf{v} = 0 \qquad (3.22)$$

which can be obtained by summing (3.8). From these, we can have a concentration equation for each species,

$$\rho(\frac{\partial \omega_i}{\partial t} + \mathbf{v} \cdot \nabla \omega_i) = -\nabla \cdot \mathbf{j}_i \ , \tag{3.23}$$

equivalently,

$$\frac{\partial \omega_i}{\partial t} + \mathbf{v} \cdot \nabla \omega_i = -\frac{1}{\rho} \nabla \cdot \mathbf{j}_i \ . \tag{3.24}$$

In (3.9), the dot product within the diffusion term is between the indices of the gradient and the divergence. The term proportional to $\mathbf{j}_i$ in (3.10) represents the diffusion of enthalpy, and is a consequence of heat flux due to mass diffusion between different species [31]. In this paper, we formulate the equations in terms of two phases. See Cheng et al. [6] for extensions of the equations below to the general multi phase case, in the incompressible limit.

For simplicity of the simulation, we assume no mass diffusion for the immiscible case and no surface tension for the miscible case. Since our examples only consider constant diffusivity for binary mixtures ($n = 2$, $\nu_{1,2} = \nu_{2,1} = \nu =$ *constant*), and constant coefficients of surface tension $\sigma =$ *constant*, a consequence of this assumption is that we only consider flows that are either purely diffusive $\sigma = 0$ and no material interfaces, or non-diffusive $\nu = 0$, sharp material interfaces, but never both simultaneously.

3.4 Averaged Equations

In this section we multiply the phase indicator function X_k by both sides of each of the equations (3.8)–(3.10), so that the equations are specified for each phase, and perform ensemble average, which is based on the ideas of Drew [11]. In this sense the averaged macroscopic equations conceptually present a chunk phase motion rather than the point-wise motion in the primitive microscopic equations. For our 3D simulation in a rectangular coordinate system here, the ensemble average is replaced a spatial average over the x_1, x_2-plane so that the average is assumed to be independent of x_1 and x_2. Even though our simulation is 3D RT in Cartesian coordinates we generalize the averaged equation in three different geometric coordinates, the planar, cylindrical and spherical ones by using the indicator $s = 0, 1, 2$, respectively. Similar to the rectangular coordinate case, we integrate the equations over the θ, or θ and z directions in cylindrical coordinates, ,over the θ or θ and ϕ directions in spherical coordinates. This yields one or two dimensional multi-phase flow averaged equations. When the equations are given in cylindrical and spherical coordinates, there are geometrical source terms due to the curvilinearity of coordinate systems [24].

We use the two types of average introduced in the previous Section 3.1. The averaged quantities $\rho_{i,k}$, ρ_k and p_k are defined as the phase average of the species i densities ρ_i, density ρ and pressure p, respectively, so that we have

$$\rho_{i,k} = \frac{\langle X_k \rho_i \rangle}{\langle X_k \rangle} \ , \quad \rho_k = \frac{\langle X_k \rho \rangle}{\langle X_k \rangle} \ , \quad p_k = \frac{\langle X_k p \rangle}{\langle X_k \rangle} \ . \tag{3.25}$$

The quantities v_k and E_k are mass-weighted averages of velocity v in the direction of z and total energy E in phase k and those are expressed by

$$v_k = \frac{\langle X_k \rho v_z \rangle}{\langle X_k \rho \rangle} \ , \quad E_k = \frac{\langle X_k \rho E \rangle}{\langle X_k \rho \rangle} \ . \tag{3.26}$$

For later use we define the three averaged interfacial quantities v^*, p_k^* and $(p_k v)^*$

by

$$v^* = \frac{\langle \mathbf{v} \cdot \nabla X_k \rangle}{\langle \mathbf{n}_3 \cdot \nabla X_k \rangle} \ , \quad p_k^* = \frac{\langle p_k \mathbf{n}_3 \cdot \nabla X_k \rangle}{\langle \mathbf{n}_3 \cdot \nabla X_k \rangle} \ , \quad (p_k v)^* = \frac{\langle p_k \mathbf{v} \cdot \nabla X_k \rangle}{\langle \mathbf{n}_3 \cdot \nabla X_k \rangle} \ , \tag{3.27}$$

By averaging the advection law (3.3) we get

$$\left\langle \frac{\partial X_k}{\partial t} \right\rangle + \langle v_{int} \cdot \nabla X_k \rangle = 0 \ , \tag{3.28}$$

which becomes by the property of ensemble average and the definition of v^* in (3.27),

$$\left\langle \frac{\partial \beta_k}{\partial t} \right\rangle + v^* \left\langle \frac{\partial \beta_k}{\partial z} \right\rangle = 0 \ , \tag{3.29}$$

where z direction is the normal direction.

Applying the ensemble average to the equations (3.8)–(3.10), we obtain the ensemble averaged equations

$$\frac{\partial(\beta_k \rho_{ki})}{\partial t} + \nabla \cdot (\beta_k \rho_{ki} \mathbf{v}_k) = \langle X_k \nabla \cdot \mathbf{j}_i \rangle \ , \tag{3.30}$$

$$\begin{aligned} &\frac{\partial(\beta_k \rho_k \mathbf{v}_k)}{\partial t} + \nabla \cdot (\beta_k \rho_k \mathbf{v}_k \mathbf{v}_k) + \nabla \cdot (\beta_k \mathbf{R}_k) \\ &= \nabla \cdot (\beta_k \tau_k) - \langle \tau \nabla X_k \rangle + \beta_k \rho_k \mathbf{g} \ , \end{aligned} \tag{3.31}$$

$$\begin{aligned} &\frac{\partial(\beta_k \rho_k E_k)}{\partial t} + \nabla \cdot (\beta_k \rho_k \mathbf{v}_k E_k) + \nabla \cdot (\beta_k \mathbf{S}_k) \\ &= \nabla \cdot \langle X_k \tau \mathbf{v} \rangle - \langle \tau \mathbf{v} \nabla X_k \rangle + \beta_k \rho_k \mathbf{v}_k \cdot \mathbf{g} + \left\langle X_k \nabla \cdot \sum_i h_i \mathbf{j}_i \right\rangle + \langle X_k \nabla \cdot \kappa \nabla T \rangle \ , \end{aligned} \tag{3.32}$$

where $\mathbf{R}_k$ is the Reynolds stress tensor and $\mathbf{S}_k$ is the turbulent flux of total energy, both for phase k,

$$\mathbf{R}_k = \frac{\langle X_k \rho \mathbf{v}\mathbf{v} \rangle}{\beta_k} - \frac{\langle X_k \rho \mathbf{v} \rangle^2}{\beta_k \langle X_k \rho \rangle} \ , \quad \mathbf{S}_k = \frac{\langle X_k \rho \mathbf{v} E \rangle}{\beta_k} - \frac{\langle X_k \rho E \rangle \langle X_k \rho \mathbf{v} \rangle}{\beta_k \langle X_k \rho \rangle} \ . \tag{3.33}$$

We note that we choose a preferred direction normal to the mixing layer (x_3 direction in 3D rectangular coordinate) and integrate the equations (3.30)–(3.32) over two other directions tangent to it ($x_1 x_2$ plane in 3D rectangular coordinate). This procedure yields one dimensional averaged equations. We follow Drew [11] and earlier papers [4, 5] to obtain

$$\frac{\partial(\beta_k \rho_{ki})}{\partial t} + \nabla^s(\beta_k \rho_{ki} v_k) = \beta_k \mathcal{D}_{ki} \ , \tag{3.34}$$

$$\frac{\partial(\beta_k \rho_k v_k)}{\partial t} + \nabla^s(\beta_k \rho_k v_k^2) = -\frac{\partial}{\partial z}(\beta_k p_k) + p_k^* \frac{\partial \beta_k}{\partial z} + \beta_k \rho_k g + \beta_k \mathcal{M}_k \ , \tag{3.35}$$

$$\frac{\partial(\beta_k \rho_k E_k)}{\partial t} + \nabla^s(\beta_k \rho_k v_k E_k) = -\nabla^s(\beta_k p_k v_k) + (p_k v)^* \frac{\partial \beta_k}{\partial z} + \beta_k \rho_k v_k g + \beta_k \mathcal{E}_k \ . \tag{3.36}$$

Summing the equation (3.34) over i, we get the equations for total mass

$$\frac{\partial(\beta_k \rho_k)}{\partial t} + \nabla^s(\beta_k \rho_k v_k) = 0 \ , \tag{3.37}$$

where

$$\nabla^s f(z) = \frac{1}{z^s} \frac{\partial z^s f(z)}{\partial z} \tag{3.38}$$

is the curvilinear divergence. For convenience, we use the following symbols to represent the source terms of (3.34)–(3.36)

$$\mathcal{D}_{ki} = (\nabla \cdot \mathbf{j}_i)_k \tag{3.39}$$

$$\mathcal{M}_k = (\nabla \cdot \tau')_{k,3} + f_k^s \ , \tag{3.40}$$

$$\mathcal{E}_k = (\nabla \cdot \tau' \mathbf{v})_k + (\nabla \cdot (\sum_i h_i \mathbf{j}_i))_k + (\nabla \cdot (\kappa \nabla T))_k \ , \tag{3.41}$$

in which $(\nabla \cdot \tau')_{k,3}$, and v_3 mean the third component of $(\nabla \cdot \tau')_k$ and $\mathbf{v}$. f_k^s is the averaged geometrical source term, that is, the averaged centrifugal forces which is expressed by

$$f_k^s = \begin{cases} 0 & s = 0 \\ \frac{1}{r}\left\langle X_k \rho v_\theta^2 \right\rangle / \beta_k & s = 1 \\ \frac{1}{r}\left\langle X_k \rho (v_\theta^2 + v_\phi^2) \right\rangle / \beta_k & s = 2 \end{cases} \tag{3.42}$$

3.5 A Closure Model

In this section we propose our closure model. As we defined in the previous section we denote the interfacial averaged quantities of p, v, pv as q^* where $q = v, p, pv$. The first step in the closure derivation is to derive an exact identity [16] from the averaged equations, which was previously derived. Here the result is extended to the multi species mass diffusion cases. The next step is to find a reasonable closure model and finally we pursue the simplest model with good approximation.

3.5.1 v^* Closure

We use the notation Z_k for the edge positions, i.e. Z_1 is the bubble edge and Z_2 is the spike edge. At each edge Z_k the velocity is denoted by $v_k = V_k$. We assume that $(-1)^k V_k = (-1)^k \dot{Z}_k \geq 0$, which means that the mixing zone is monotonously growing *i.e.* both pure phase fluids are constantly coming into the mixing zone so that the volume of the mixing zone is increasing. The interfacial velocity v^* at the both edges satisfies a boundary condition.

$$v^* = \dot{Z}_k = v_k \quad \text{at} \quad z = Z_k \tag{3.43}$$

The exact expression for the interface velocity v^* can be directly derived from the previous averaged equations (3.29) and (3.37) by using the definition of v^* in (3.27). Dividing (3.37) by ρ_k and subtracting the result from (3.29), to obtain

$$(v_k - v^*) \frac{\partial \beta_k}{\partial z} + \beta_k \left[\nabla^s v_k + H_k^v \right] = 0 \ , \tag{3.44}$$

where

$$H_k^v \ = \ \frac{1}{\rho_k} \frac{D_k \rho_k}{Dt} \ . \tag{3.45}$$

Here D_k/Dt is the substantive derivative with respect to the velocity v_k. We sum (3.44) over k, solve for $\partial \beta_k / \partial z$, and substitute the result in (3.44). The following theorem gives us the algebraically simplified expression.

Theorem 3.1. *The interface quantity v^* has the exact formula*

$$v^* = \mu_1^v v_2 + \mu_2^v v_1 \ , \tag{3.46}$$

where the mixing coefficients have the fractional linear form

$$\mu_k^v = \frac{\beta_k}{\beta_k + d_k^v \beta_{k'}} \ . \tag{3.47}$$

The constitutive factor d_k^v is also expressed in the exact form

$$d_k^v(z,t) = \frac{\nabla^s v_{k'} + H_{k'}^v}{\nabla^s v_k + H_k^v} \ . \tag{3.48}$$

The factor $d_k^v(z,t)$ in (3.48) can be interpreted as a ratio of logarithmic rates of volume creation for the two phases.

With spatial homogeneity we define

$$d_k^v(t) = \frac{\displaystyle\int_{Z_k}^{Z_{k'}} \frac{\partial (z^s v_{k'})}{\partial z} + z^s H_{k'}^v dz}{\displaystyle\int_{Z_k}^{Z_{k'}} \frac{\partial (z^s v_k)}{\partial z} + z^s H_k^v dz} \ , \tag{3.49}$$

which shows that the relative extent of volume creation for the two fluid species do not depend on the spatial location in the mixing zone, which means this closure is independent of the exact expression (3.48). The ratio (3.49) satisfies the relation $d_1^v(t)d_2^v(t) = 1$ which is equivalent to $\mu_1^v + \mu_2^v = 1$. Furthermore, $d_k^v(t) \geq 0$ if and only if μ_k^v is nonnegative finite for $0 \leq \beta_k \leq 1$.

Before we specify a simple choice for the quantity $d_k^v(t)$, we here discuss sensitivity of the choice. We proposed an inequality as a criteria which is

$$|\Delta q| \equiv |q_1 - q_2| \ll |\overline{q}| \equiv |\beta_1 q_1 + \beta_2 q_2| \quad q = v, \ p \ . \tag{3.50}$$

If (3.50) is not satisfied then the closure $q^* \partial \beta_k / \partial z$ is sensitive to the choice of $d_k^q(t)$. For the v^* closure which violates (3.50), the light fluid moves away from the direction of g and the heavy fluid moves in the direction of g. Thus in most parts of the mixing zone, v_1 and v_2 has opposite signs, so that $\overline{v}$ is nearly zero relative to Δv, or in other words, Δv is large.

In Figure 3.3, we see the optimized $d_k^v(t)$ to minimize the relative error where

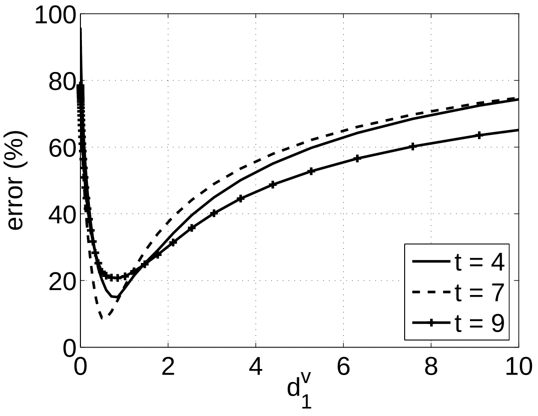

Figure 3.3: The sensitivity of $v^* \partial \beta_1 / \partial z$ with different choice of $d_k^v(t)$

the error is defined as

$$\text{error} = \frac{\int |\text{data} - \text{model}|\, dz}{\int |\text{data}| dz} \tag{3.51}$$

at each time $t = 4, 7, 9$. The integration extends over the mixing zone. The sensitivity of v^* can be interpreted as follows.

Also $d_k^v > 0$ is noticeable, which means the unmixed pure phase fluids are entrained into the mixture of the two fluids, which rises the V_k terms in (3.49) and also the relative compression of the two densities affects on the logarithmic substantive derivative terms in (3.49)). In this sense our simple closure form of d_k^v is

$$d_k^v(t) = \left(\frac{Z_{k'}}{Z_k} \right)^s \left| \frac{V_{k'}}{V_k} \right| \ . \tag{3.52}$$

This is clearly seen in the incompressible, non-diffusive RT case since the second terms in the numerator and the denominator of the identity (3.49) degenerate. This solution (3.52) is a consequence of the closed form expression obtained for the solution of the model equations and a simple calculation [17–19]. In Figure 3.4, we plot the closed $d_k^v(t)$ vs. t, for all of our different RT data sets.

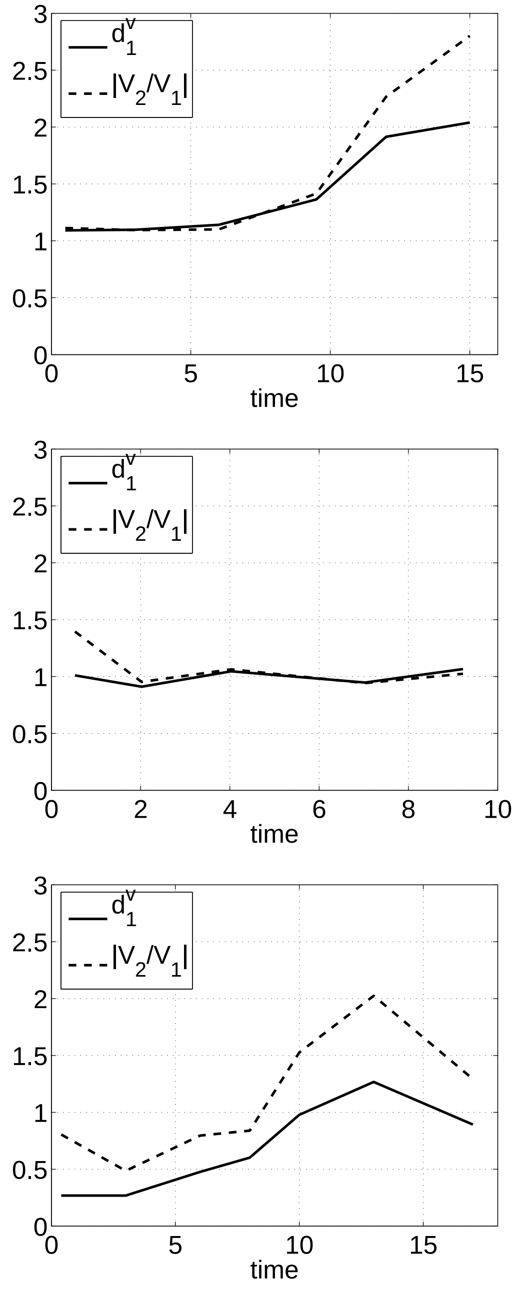

Figure 3.4: The closed quantity $d_1^v(t)$ from (3.49) compared to the value from (3.52) for 3D RT data. Left to right: ideal, surface tension and mass diffusion data.

3.5.2 p^* Closure

In the case of non-zero surface tension, pressure is discontinuous at the interface ∂X_k, and p_k is the value of the pressure defined by continuity from the interior of X_k. These limiting pressures at the micro physical level, i.e. before ensemble averaging, are related by the equation

$$p_1 - p_2 = (K\sigma\mathbf{n} + \nabla_{\|}\sigma) \cdot \mathbf{n} + \mathbf{n}^T[\tau']\mathbf{n} = K\sigma + \mathbf{n}^T[\tau']\mathbf{n} \tag{3.53}$$

where K is the mean curvature and σ is the surface tension. At the interface of two fluids, the jump condition is

$$[\mathbf{T}^T\mathbf{n}] = -\sigma K\mathbf{n} - \nabla_{\|}\sigma, \tag{3.54}$$

in which the symbol $[\cdot]$ is defined as $[f] = f_1 - f_2$ and $\nabla_{\|} = (\mathbf{I} - \mathbf{nn}) \cdot \nabla$ is the surface tangential component of the gradient. This shows a balance of forces law. Here σ is the coefficient of surface tension. The unit normal vector $\mathbf{n}$ is directed into fluid 1. We use the mean curvature

$$K = \kappa_1 + \kappa_2 \ , \tag{3.55}$$

where κ_1 and κ_2 are the maximum and minimum curvatures, and are positive when pointing into fluid 1. The first term in (3.54) shows the classical surface tension. The second term in (3.54) is the Marangoni force, which is the tangential force on the surface generated by a concentration dependence of the surface tension. It is convenient to define

$$p^* = \frac{1}{2}(p_1^* + p_2^*) \ , \tag{3.56}$$

and the capillary pressure

$$p_c^* = p_1^* - p_2^* \ , \tag{3.57}$$

where p_k^* is pressure of phase k at the front state, so that

$$p_1^* = p^* + \frac{p_c^*}{2} \ , \quad p_2^* = p^* - \frac{p_c^*}{2} \ . \tag{3.58}$$

In view of (3.53), p_c^* is the product of the surface tension σ and the average of the surface mean curvature. Similarly we define $(pv)^*$ and $(p_c v)^*$ as the average and the difference of the $(p_k v)^*$. We then define

$$\widetilde{p_k} \ = \ p_k + (-1)^k \frac{p_c^*}{2} \tag{3.59}$$

$$\widetilde{p_k^*} \ = \ p_k^* + (-1)^k \frac{p_c^*}{2} = p^* \ . \tag{3.60}$$

The required boundary condition (3.43) for p^* at the mixing zone edge Z_k can be reformulated as

$$\widetilde{p_k} = \widetilde{p_k^*} = p^* \quad \text{at} \quad Z_k \ . \tag{3.61}$$

We derive an exact expression for p^* in terms of other solution variables. This exact form will be approximated to yield a closed expression for p^*. We start by subtracting v_k times (3.37) from (3.35) to obtain

$$\beta_k(\frac{\partial p_k}{\partial z} - H_k) + (\widetilde{p_k} - p^*)\frac{\partial \beta_k}{\partial z} = 0 \ , \tag{3.62}$$

where

$$H_k = \rho_k \left(g - \frac{D_k v_k}{Dt} - \frac{\mathcal{M}_k}{\rho_k} \right) \ . \tag{3.63}$$

Adding the two equations (3.62) for $k = 1, 2$, we obtain

$$(\widetilde{p_2} - \widetilde{p_1})\frac{\partial \beta_1}{\partial z} = \beta_1\left(\frac{\partial p_1}{\partial z} - H_1\right) + \beta_2\left(\frac{\partial p_2}{\partial z} - H_2\right) \ , \tag{3.64}$$

since the p^* terms cancel when summed over k. Equation (3.64) is substituted into (3.62) and the result is solved for p^*, yielding

$$p^* - \widetilde{p_1} = \frac{(\widetilde{p_2} - \widetilde{p_1})\beta_1\left(\frac{\partial p_1}{\partial z} - H_1\right)}{\beta_1\left(\frac{\partial p_1}{\partial z} - H_1\right) + \beta_2\left(\frac{\partial p_2}{\partial z} - H_2\right)} \ . \tag{3.65}$$

This expression can be simplified to give the following theorem.

Theorem 3.2. *The interface pressure p^* is expressed exactly as*

$$\begin{aligned} p^* &= \frac{\beta_1\left(\frac{\partial p_1}{\partial z} - H_1\right)\widetilde{p_2} + \beta_2\left(\frac{\partial p_2}{\partial z} - H_2\right)\widetilde{p_1}}{\beta_1\left(\frac{\partial p_1}{\partial z} - H_1\right) + \beta_2\left(\frac{\partial p_2}{\partial z} - H_2\right)} && (3.66) \\ &\equiv \mu_1^p\widetilde{p_2} + \mu_2^p\widetilde{p_1} \ , && (3.67) \end{aligned}$$

where the mixing coefficients μ_k^p satisfy

$$\mu_k^p = \frac{\beta_k}{\beta_k + d_k^p\beta_{k'}} \ . \tag{3.68}$$

The constitutive coefficients d_k^p are obtained in the exact form

$$d_k^p(z,t) = \frac{\frac{\partial p_{k'}}{\partial z} - H_{k'}}{\frac{\partial p_k}{\partial z} - H_k} \ , \tag{3.69}$$

This coefficient (3.69) represents a ratio of the forces accelerating the two fluids, each considered in the accelerated frame defined by their respective velocities. The first derivative term in this coefficients d_k^p represents the acceleration from the pressure and the H_k term does that from gravity and inertial forces. Unless $H_k = \partial p_k / \partial z$ which is hydrostatic equilibrium, there must be a deviation between these forces. If the deviation is positive the total force supplies extra acceleration to the phase k, otherwise it decreases the total acceleration. Figure 3.5 shows each force. The result is a net decrease in the downward acceleration of the light fluid and a net increase in the upward acceleration of the heavy fluid, which causes $d_k^p < 0$ and $|Z_1| < |Z_2|$. This provides that the spike growth rate is bigger than the bubble growth rate in general. Also in the same figure we can see the possibility that the coefficient d_k^p can be negative so that the denominator of μ_k^p is zero, which causes blow-ups in our $p^* \partial \beta_1 / \partial z$ closure.

Figure 3.6 presents the distribution of those zero roots (denoted z^*). One of our trial and error method to find a closure model was to use these points. In other words, we used $d_k^p(z^*, t)$ for our closure model. Mathematically, if we plug these zero roots in the numerator and the denominator those are supposed to be cancelled by using L'hospital's rule. But it is a mistake if we do not consider the numerical error. Since we have a finite grid size, the numerator and denominator are closely but not exactly zeros so that those are not exactly cancelled out and make considerably big blow-ups. Figure 3.7 and Table 3.5.2 gives a quick view of the error when we use those $d_k^p(z^*, t)$. Also the zeros do not have any special pattern so that it is hard to keep away from this problem with the negative d_k^p causing the blow-ups of closure model.

This leads us to force d_k^p to be positive. Surprisingly the choice is not a matter once it is positive. Figure 3.8 shows the insensitivity of the closure with any choice of d_k^p which is the opposite property of v^* closure in Figure 3.3. For definiteness, we set $d_k^p = 1$, for example. The $d_k^p(t)$ satisfies the relation $d_1^p(t) d_2^p(t) = 1$ which is equivalent to $\mu_1^p + \mu_2^p = 1$.This insensitivity can also be seen clearly seen in Figure 3.9.

As the two fluids are mixing the pressures from the two fluids have a tendency of

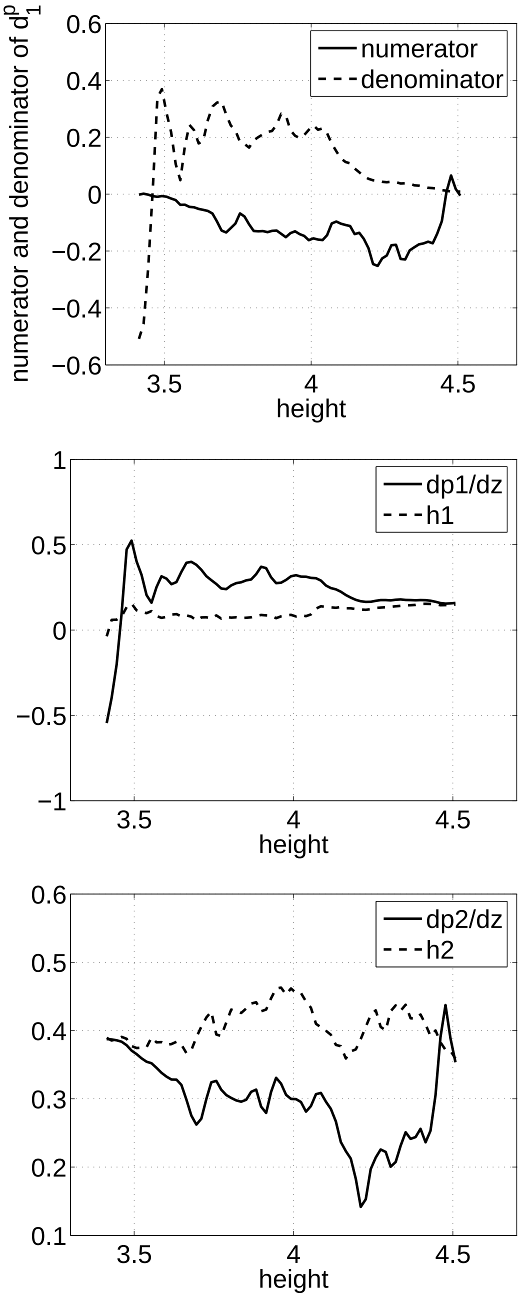

Figure 3.5: Top: the numerator and denominator of the exact $d_1^p(z,t)$ in the mixing zone at 9, using (3.69). Center and bottom: the first terms $\partial p_k/\partial z$ and the second terms H_k of the numerator and denominator at $t = 4$ (top) and 9 (bottom).

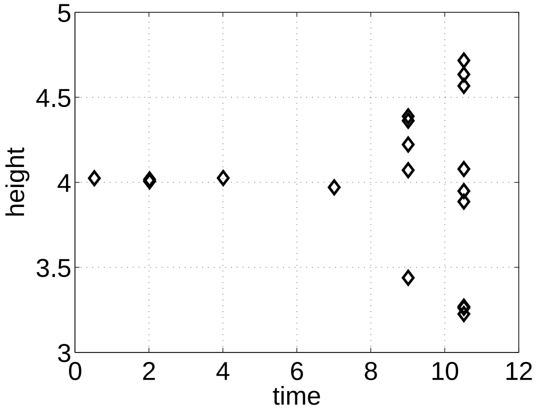

Figure 3.6: The distribution of the zeros z^* of the denominator of $p^* \frac{\partial \beta_1}{\partial z}$.

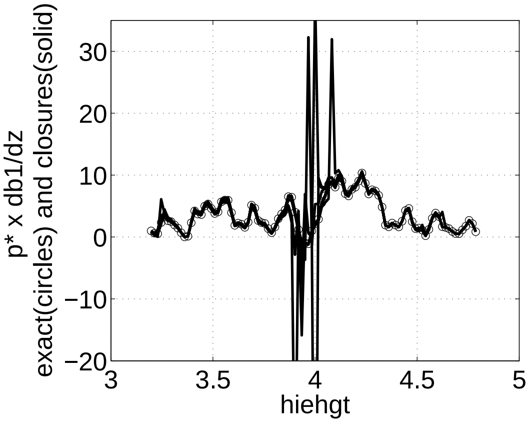

Figure 3.7: $p^* \frac{\partial \beta_1}{\partial z}$ with $d_k^p(t) = d_k^p(z^*, t)$ for all z^* at time $t = 11$ with RT surface tension data.

Surface Tension Data with Surface Tension Terms in Formula

Time	z^*	d_1^p	d_2^p	*Error (Percent)*
0.5230	4.0238	-2524.8900	-0.0004	2.8773
2.0162	4.0057	-2.5428	-0.3933	0.5071
	4.0068	-3.0103	-0.3322	12994e+11
	4.0169	-12.9310	-0.0773	2.8773
4.0089	4.0252	-0.1732	-5.7735	5.3268
7.0110	3.9700	-0.6640	-1.5059	85.1186
9.0106	3.4385	-0.0073	-136.5730	2.7482
	4.0708	-0.9761	-1.0244	3.2501
	4.2221	-4.8075	-0.2080	14.1469
	4.3623	-13.5136	-0.0740	28.1431
	4.3878	-15.8326	-0.0632	2.7544
10.5159	3.2253	-0.0097	-102.8710	2.1730
	3.2610	-0.0239	-41.8760	3.5820
	3.2686	-0.0280	-35.659	4.9875
	3.8862	-0.6326	-1.5807	77.0612
	3.9478	-0.6828	-1.4646	180.9100
	4.0779	-0.9366	-1.0678	1074.7000
	4.5665	-12.5414	-0.0797	23.2765
	4.6345	-24.1695	-0.0414	47.4109
	4.71613	-37.0335	-0.0270	10.8158

Table 3.1: The error analysis of the closure $p^*\frac{\partial \beta_1}{\partial z}$ with $d_k^p(z^*,t)$

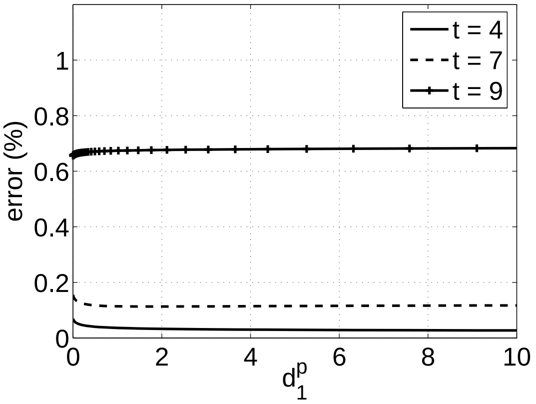

Figure 3.8: The sensitivity of $v^*\partial\beta_k/\partial z$ with different choice of $d_k^p(t)$

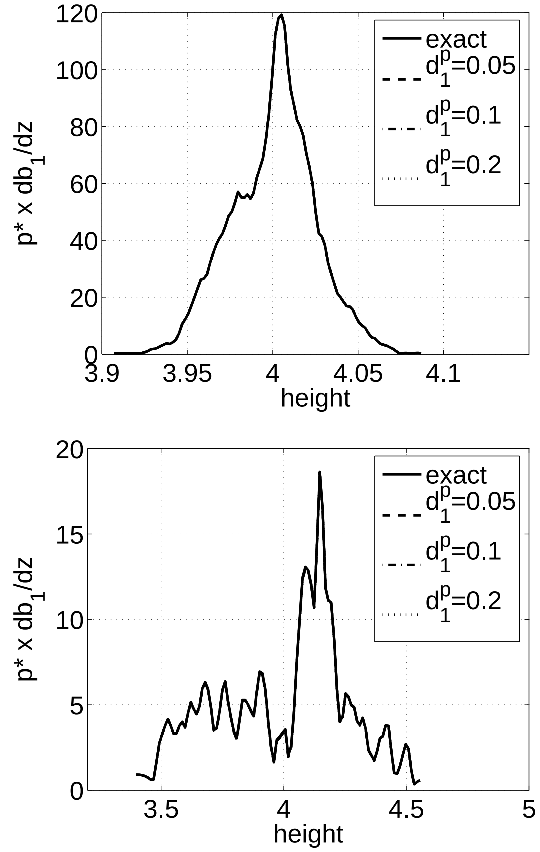

Figure 3.9: The exact quantity $p^*\partial\beta_1/\partial z$ with (3.66) and closed quantity $p^*\partial\beta_1/\partial z$ defined by (3.67) for 3 choices of d_k^p at $t = 4$ (top) and $t = 9$ (bottom). The four curves are indistinguishable.

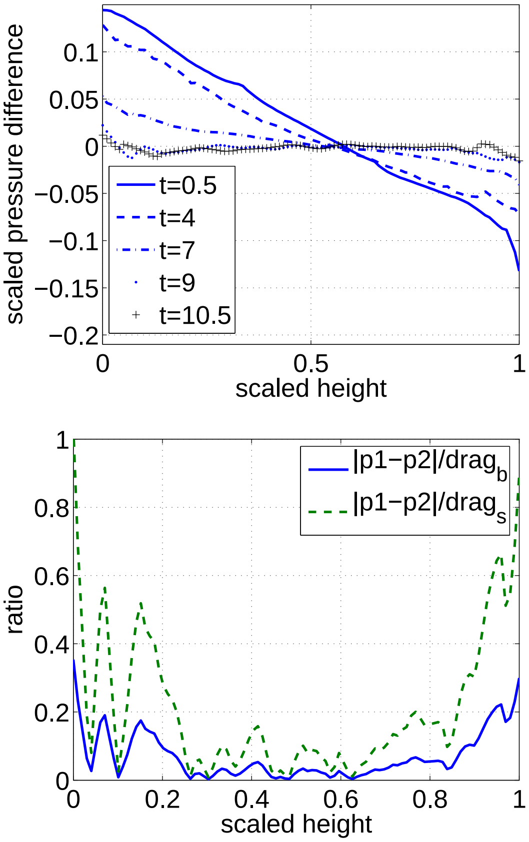

Figure 3.10: Left: the scaled pressure difference $\Delta\widetilde{p}/(Z_2-Z_1)$ is plotted *vs*. the scaled height $(z-Z_1)/(Z_2-Z_1)$ at $t = 0.5,\ 2,\ 4,\ 7,\ 9$ for the 3D RT surface tension data. Right: the ratio of pressure difference and unit drag force $\rho_{k'}(\Delta v)^2/(Z_2-Z_1)$ at $t = 9$.

equilibration. This tendency is stronger in late time and eventually a central portion of the mixing zone satisfies $\Delta\tilde{p} \approx 0$, which can bee seen in Figure 3.10 top frame, where we show pressure differences scaled by the mixing zone length. In the right frame, we scale this difference by a unit drag force which is $\rho_{k'}(\Delta v)^2/(Z_2 - Z_1)$. We see the pressure difference is significant near the edges of the mixing zone. This can also support the insensitivity of the closure to the choice of $d_k^p(t)$ by satisfying the inequality (3.50).

3.5.3 $(pv)^*$ Closure

In the case with surface tension, the work associated with limiting pressures is not continuous at the interface as stated at the beginning of the previous section 3.5.2. From (3.53), we have

$$(p_1 v)^* - (p_2 v)^* = (p_c v)^* \ . \tag{3.70}$$

We derive a mathematically exact expression for $(pv)^*$ using an entropy formulation. From (3.34) and (3.35), we get the kinetic energy equation

$$\begin{aligned} & \frac{\partial}{\partial t}\left(\beta_k \rho_k \frac{v_k^2}{2}\right) + \nabla^s\left(\beta_k \rho_k v_k \frac{v_k^2}{2}\right) \\ = \ & v_k \left[-\frac{\partial(\beta_k p_k)}{\partial z} + p_k^* \frac{\partial \beta_k}{\partial z} + \beta_k \rho_k g + \beta_k \mathcal{M}_k \right] . \end{aligned} \tag{3.71}$$

Subtracting (3.71) from (3.36), we have the internal energy equation

$$\begin{aligned} & \frac{\partial}{\partial t}\left(\beta_k \rho_k e_k\right) + \nabla^s\left(\beta_k \rho_k v_k e_k\right) \\ = \ & -\beta_k p_k \nabla^s v_k - p_k^* v_k \frac{\partial \beta_k}{\partial z} + (p_k v)^* \frac{\partial \beta_k}{\partial z} + \beta_k \mathcal{F}_k \ , \end{aligned} \tag{3.72}$$

where

$$\mathcal{F}_k \ = \ \mathcal{E}_k - v_k \mathcal{M}_k \ . \tag{3.73}$$

We define $\mathbb{S}_k$ to be the entropy defined by the averaged variables E_k and ρ_k using the equation of state and we define S_k to be the direct ensemble average of the micro physically defined phase entropy. The process of averaging (forming the ensemble average) is not adiabatic, that is, the entropy is not conserved by the averaging process, so that $\mathbb{S}_k \neq S_k$ in general. Besides, we expect the averaging to satisfy an entropy inequality, leading to $\mathbb{S}_k \geq S_k$. For an adiabatic process, $dS_k = 0$ and $d\mathbb{S}_k = d(\mathbb{S}_k - S_k)$.

We assume the thermodynamic relation is satisfied for the averaged quantities

$$T_k d\mathbb{S}_k = de_k + p_k d\left(\frac{1}{\rho_k}\right) . \tag{3.74}$$

From (3.72) and (3.74), we derive the entropy equation

$$\beta_k \rho_k T_k \frac{D\mathbb{S}_k}{Dt} = [-p_k v^* + p_k v_k - p_k^* v_k + (p_k v)^*] \frac{\partial \beta_k}{\partial z} + \beta_k \mathcal{F}_k \ . \tag{3.75}$$

We define

$$(\overline{p_k} v) = \widetilde{p_k} v_k + \frac{(-1)^k}{2} [p_c^* v^* - (p_c v)^*]. \tag{3.76}$$

(3.75) can be reformulated as

$$\beta_k \rho_k T_k \frac{D\mathbb{S}_k}{Dt} = [-\widetilde{p_k} v^* - p^* v_k + (\overline{p_k} v) + (pv)^*] \frac{\partial \beta_k}{\partial z} + \beta_k \mathcal{F}_k, \tag{3.77}$$

Solving (3.77) for $(pv)^*$ yields

Theorem 3.3. *$(pv)^*$ is expressed exactly as*

$$\begin{aligned} (pv)^* \ &= \ p^* \left(\mu_1^{pv} v_2 + \mu_2^{pv} v_1\right) + v^* \left(\mu_1^{pv} \widetilde{p_2} + \mu_2^{pv} \widetilde{p_1}\right) \\ &\quad - \left(\mu_1^{pv} (\overline{p_2} v) + \mu_2^{pv} (\overline{p_1} v)\right) \ . \end{aligned} \tag{3.78}$$

where the mixing coefficients μ_k^{pv} satisfy

$$\mu_k^{pv} = \frac{\beta_k}{\beta_k + d_k^{pv} \beta_{k'}} \ . \tag{3.79}$$

The constitutive coefficients d_k^{pv} *can be obtained in the exact form*

$$d_k^{pv}(z,t) = \frac{\rho_{k'} T_{k'} \dfrac{D_{k'} \mathbb{S}_{k'}}{Dt} - \mathcal{F}_{k'}}{\rho_k T_k \dfrac{D_k \mathbb{S}_k}{Dt} - \mathcal{F}_k} \ . \tag{3.80}$$

The process of ensemble averaging increases the entropy of the system, a process we call the positive entropy of averaging property. When the source term $\mathcal{F}_k = 0$, we expect the entropy of averaging is positive [20], which leads to the following theorem.

Theorem 3.4. *Assume the closures (3.46), (3.67) and (3.78) for* v^*, p^* *and* $(pv)^*$. *Then the inequality*

$$[(\mu_1^v - \mu_2^p)\Delta\widetilde{p}\Delta v + (p_c v)^* - p_c^* v^*] \frac{\partial \beta_1}{\partial z} \geq 0 \ . \tag{3.81}$$

is a necessary and sufficient condition for the entropy of averaging inequality for the $k = 1$ *and* $k = 2$ *fluids.*

By imposing homogeneity on (3.80) just as before, the closure becomes

$$d_k^{pv}(t) = \frac{\displaystyle\int_{Z_k}^{Z'_k} \rho_{k'} T_{k'} \frac{D_{k'} \mathbb{S}_{k'}}{Dt} - \mathcal{F}_{k'} dz}{\displaystyle\int_{Z_k}^{Z'_k} \rho_k T_k \frac{D_k \mathbb{S}_k}{Dt} - \mathcal{F}_k dz} \ . \tag{3.82}$$

Similar to the $p^* \partial\beta_1/\partial z$ closure, the closure for $(pv)^* \partial\beta_1/\partial z$ is also insensitive to the choice of d_1^{pv}, in view of the criteria (3.50). Figure 3.11 shows the property as well. The first and the third terms in (3.78) nearly cancel each other, so that the insensitivity comes from that of p^* and also it must depend on v^*. That is,

$$(pv)^* \approx p^* v^* \ . \tag{3.83}$$

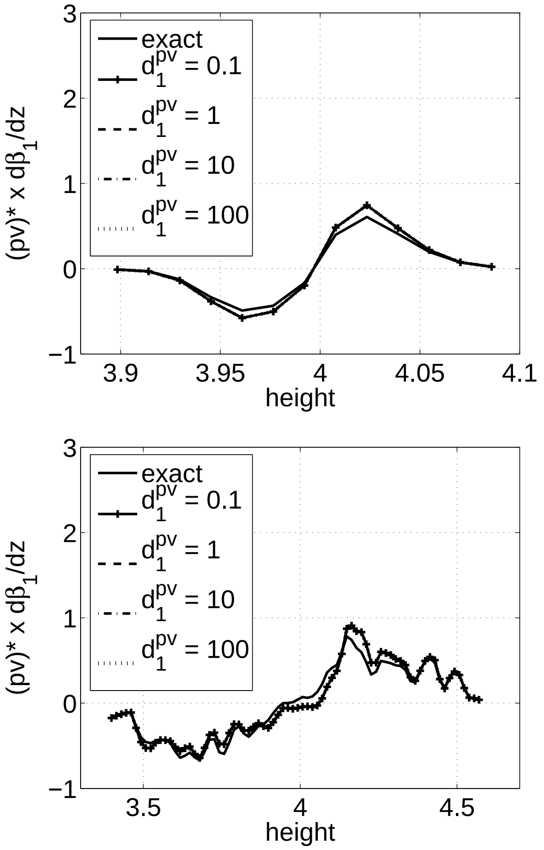

Figure 3.11: The exact quantity $(pv)^*\partial\beta_1/\partial z$ for the 3D RT data set, with (3.78) and the closed quantity $(pv)^*\partial\beta_1/\partial z$ defined by (3.78), (3.79) for $d_1^{pv} = 0.1, 1.0, 10, 100$ at early time, $t = 4$ (left) and at late time $t = 9$ (right).

3.6 Another Closure Model and Comparison

We introduce a similar work by Saurel and coworkers. As we mentioned in the previous sections we denote the interfacial averaged quantities of p, v, pv for our model, in general, q^* where $q = v, p, pv$. For the work by Saurel et al., we use q^{S*} instead. Two versions of closure models are introduced. In recent work by Saurel et al. [7] they introduce the relaxation coefficients coming from phase interaction and adopt Discrete Equations Method (DEM) to a micro structure and obtain a system of PDEs as the continuous limit of the discrete equations. The analysis starts with mass, momentum and energy equation with pure relaxation term in momentum and energy equations as source terms. Also the relaxation term is added to the averaged advection equation. There are two versions of models, introduced here, with and without the relaxation terms.

Before applying the relaxation terms in the equations their closure, a related but different functional form for their closure model is obtained. Similar to our closure they also consider a convex sum

$$q'^{S*} = \mu_1^{Sq} q_2 + \mu_2^{Sq} q_1 \quad q = v, p \ , \tag{3.84}$$

and then define

$$v^{S*} = v'^{S*} + \operatorname{sgn}\left(\frac{\partial \beta_1}{\partial x}\right) \frac{p_2 - p_1}{\mathcal{Z}_1 + \mathcal{Z}_2} \ , \tag{3.85}$$

$$p^{S*} = p'^{S*} + \operatorname{sgn}\left(\frac{\partial \beta_1}{\partial z}\right) \left(\frac{\mathcal{Z}_1 \mathcal{Z}_2}{\mathcal{Z}_1 + \mathcal{Z}_2}\right) (v_2 - v_1) \ . \tag{3.86}$$

Here $\mathcal{Z}_k$ is the acoustic impedance of fluid k. Also

$$(pv)^{S*} = p^{S*} v^{S*} \ . \tag{3.87}$$

The other version of Saurel closures include relaxation, as an additional term in the right hand side of the associated volume fraction, momentum and energy equations. The terms for $k = 1$ are precisely

$$\mu^S(p_1 - p_2) \quad \text{volume fraction source term} \tag{3.88}$$

$$\lambda^S(v_2 - v_1) \quad \text{momentum source term} \tag{3.89}$$

$$\lambda^S v'^{S*}(v_2 - v_1) - \mu^S p'^{S*}(p_1 - p_2) \quad \text{energy source term} \tag{3.90}$$

and for $k = 2$, the momentum and energy source terms have the opposite sign. Here

$$\mu^S = \frac{A_I}{2(\mathcal{Z}_1 + \mathcal{Z}_2)} \ , \quad \lambda^S = \mu \mathcal{Z}_1 \mathcal{Z}_2 \ , \tag{3.91}$$

where A_I is the interfacial area per unit volume. In (3.88), we observe that the Δv contribution to the relaxation terms is larger than the Δp contribution, and as Δv occurs in the p^* relaxation, the p^* relaxation terms are generally significant while the v^* relaxation terms (proportional to Δp) are not.

The convex coefficient μ_k^{Sq} also has a fractional linear form

$$\mu_k^{Sq} = \frac{1}{1 + d_k^{Sq}} \ , \quad q = v, p \tag{3.92}$$

while that of ours μ_k^q has the form

$$\mu_k^q = \frac{\beta_k}{\beta_k + d_k^q \beta_{k'}} \ , \quad q = v, p, pv \tag{3.93}$$

It is common to both models that the μ_k^q and μ_k^{Sq} thus depend on a single parameter d_k^q or d_k^{Sq}. Their coefficients can be calculated as

$$d_k^{Sv} = \mathcal{Z}_k/\mathcal{Z}_{k'} \quad d_k^{Sp} = \mathcal{Z}_{k'}/\mathcal{Z}_k \ , \tag{3.94}$$

which are derived from solutions of approximate (linearized) Riemann problems modeling multi phase flows at the sub-grid level but their closure does not satisfy (3.43). The Saurel et al. model supplies the missing internal boundary conditions at the edges of the mixing zone by imposition of equal pressures $p_1(z = Z_k) = p_2(z = Z_k)$ [29].

We have two interpretations of the Saurel et al. model. In the first, which we denote as Saurel-1, A_I is regarded as a fitting parameter. The second interpretation of their model takes advantage of the fact that A_I is a computed quantity in our data, and uses this time dependent value in the definition of the model. We denote this model as Saurel-2. A_I is plotted as a function of time in Figure 3.12, to complete the definition of the Saurel-2 closure. We note that A_I has the dimensions of an inverse length and takes on large values at early time as the mixing layer tends to its (small) initial amplitude.

The Figures 3.13, 3.14 and 3.15 present the comparison of three closure models with surface tension simulation, where 'exact 'in the legend of each figure means the exact expression directly derived from the averaged equations. In these figure, we can easily conclude that for $v^*\partial\beta_1/\partial z$ and $pv^*\partial\beta_1/\partial z$, our closure model is noticeably better while for $p^*\partial\beta_1/\partial z$ both our closure and the Saurel-1 (which has the fractional linear portion of the Saurel et al. closure) give a good approximation.

To compare these models, ours and Saurel et al.'s more explicitly, we use an error

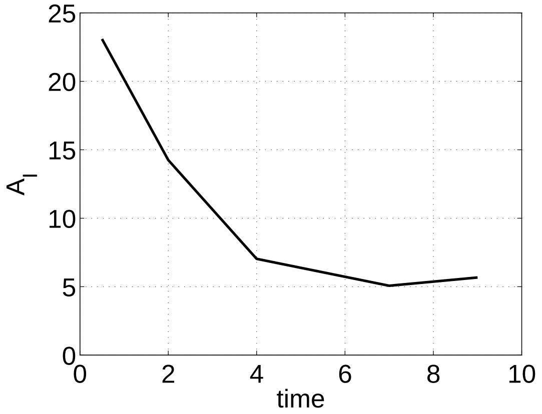

Figure 3.12: The interfacial area A_I per unit volume plotted vs. time. This plot serves to define the parameter A_I for the closure Saurel-2.

formula similar to (3.51), but including a sum over the three quantities $v^*, p^*, (pv)^*$,

$$\text{total error} = \frac{1}{3} \sum_{v^*,p^*,(pv)^*} \frac{\int\int |\text{data} - \text{model}|\, dzdt}{\int\int |\text{data}| dzdt} \ . \tag{3.95}$$

This total relative error is presented in Figure 3.16. Our main conclusion from this figure is the fact of excellent (about 10%) agreement of our closures with the simulation data. Also in the same figure, we show the dependence of the total relative error on the value assumed for the area A_I. The error is minimized for $A_I = 0$. With the choice of A_I for the Saurel-1, we compare the total relative errors in Table 3.2. In summary, our model has errors about one quarter to one half the size of those for the Saurel et al model.

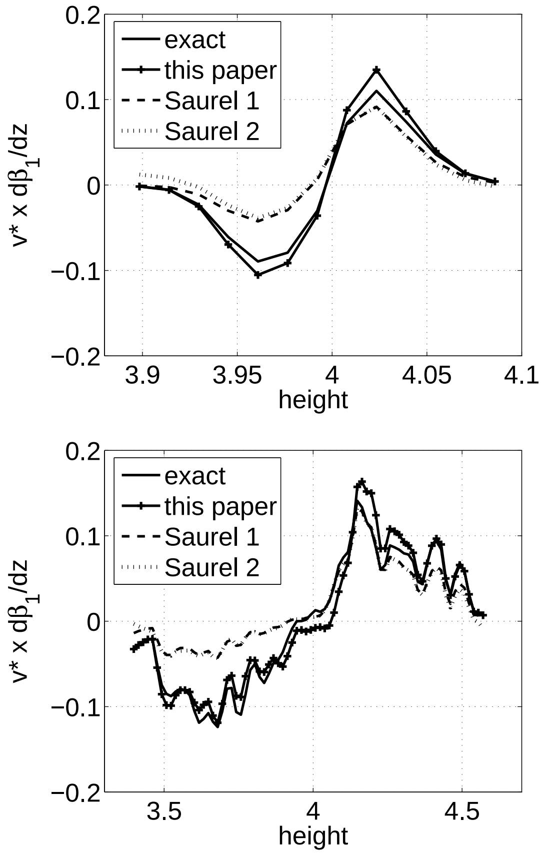

Figure 3.13: The exact quantity $v^*\partial\beta_1/\partial z$ for the 3D RT surface tension data set, with (3.44), for $k = 2$, and the closed quantity $v^*\partial\beta_1/\partial z$ defined by (3.52) in the mixing zone at an early time, $t = 4$ (left) and a late time, $t = 9$ (right). We show closure of this paper and two interpretations of the closures of Saurel et al.

Closure	v^*	p^*	$(pv)^*$	Average
	Comparison to RT data			
This paper	18%	00%	18%	12%
Saurel-1	43%	02%	42%	30%
Saurel-2	56%	46%	51%	51%

Table 3.2: Model errors based on comparison to simulation data.

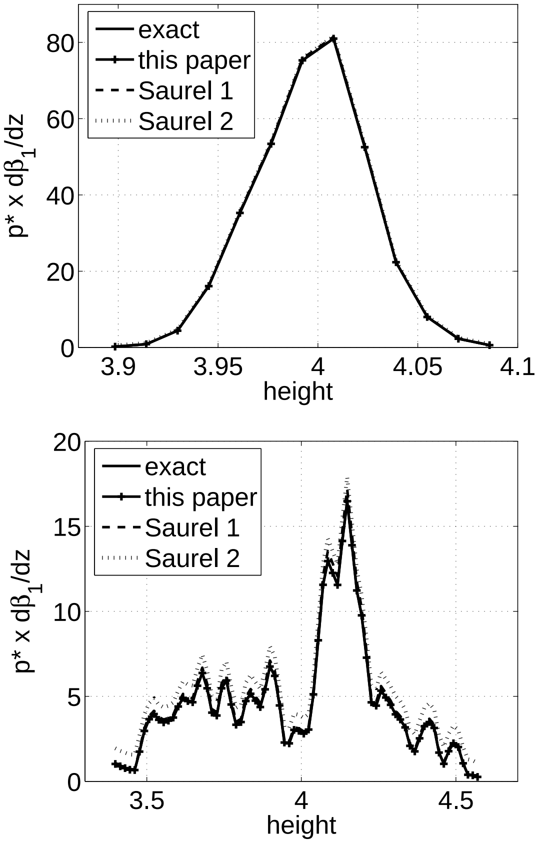

Figure 3.14: The exact quantity $p^*\partial\beta_1/\partial z$ for the 3D RT surface tension data set, with (3.69) and closed quantity $p^*\partial\beta_1/\partial z$ defined by (3.66) in the mixing zone at an early time, $t = 4$ (left) and a late time, $t = 9$ (right). We show one closure from this paper and two interpretations of the Saurel et al closures.

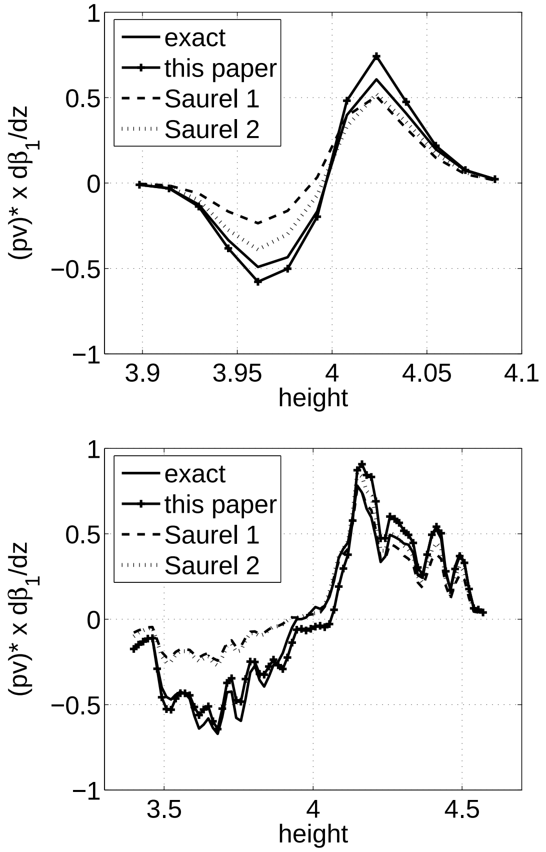

Figure 3.15: The exact quantity $(pv)^*\partial\beta_1/\partial z$ for the 3D RT data set, with (3.78) and closed quantity $(pv)^*\partial\beta_1/\partial z$ defined by (3.78), (3.79) and $d_1^{pv} = 0.1$ in the mixing zone at early time, $t = 4$ (left) and at late time $t = 9$ (right). We show the closure from this paper and two interpretations of the Saurel et al closures.

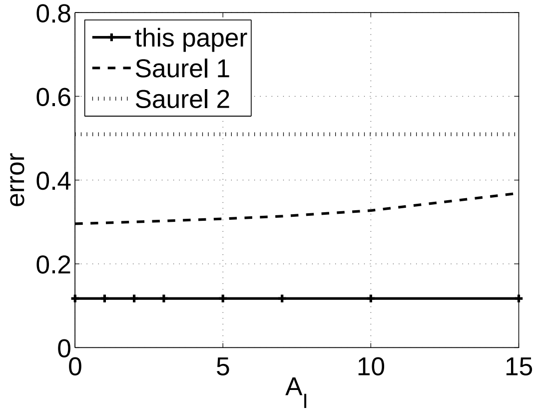

Figure 3.16: Comparison of the model error (3.95) for three closures. Of these, only Saurel-1 depends on the value of A_I as a fitting parameter; these plots serve to locate the best fit value of A_I ($A_I = 0$) and thus to define the Saurel-1 closure.

Chapter 4

Turbulent Flow Analysis

The purpose of this chapter is to analyze our data based on classical turbulence concepts including common measures of mixing properties. We introduce several parameters to measure the average degree of mixing of the two fluid systems and compare our values with those already known. For spectral analysis we start with basic definitions and see a possible approximate agreement with Kolmogorov theory. A characteristic upturn in the spectra at high wave numbers leads us to consider a subgrid model, we especially consider Smagorinsky subgrid model. But the detail analysis for the subgrid model should be in future work.

4.1 Mixing Parameters

In Chapter 2, we studied the bubble growth rate α and its statistical values. In the expression (2.5) the Atwood number is treated as a constant, $A = (\rho_2 - \rho_1)(\rho_2 + \rho_1)$, which is independent of time. Here we consider a time dependent Atwood number $A(t)$ previously defined in [14]. The time dependent Atwood number $A(t)$ measures the density contrast within the bubble portion of the mixing zone. Precisely, the local Atwood number $A(x_3, t)$ is obtained by choosing representative heavy and light density values and replacing ρ_1, ρ_2 in the previous Atwood number expression with these values, respectively, over a specific height x_3 at time t. The time dependent Atwood number $A(t)$ is defined as an average over the top half of the bubble region of local Atwood number $A(x_3, t)$. In fact, the previous constant Atwood number A in Chapter 2 is the local Atwood number of the initial mixing layer at time $t = 0$. The renormalized bubble growth rate α_{ren} can be defined by

$$\alpha_{\mathrm{ren}} = h/[2\int_0^t \int_0^s A(s_1) g ds_1 ds] \ . \tag{4.1}$$

These mixing parameters, $A(t)$ and α_{ren} are sensitive to extreme within the density contrast.

We denote the point-wise values as a zero-mesh block average, *i.e.* without averaging in the definition of the volume fraction. To study the molecular mixing fraction, we introduce a mixing or averaging length, and average the fluids over this length scale, starting with the length of one mesh block. This leads to the volume fraction, f_1, of the light fluid, calculated (in a possibly sharp interface front tracking simulation) as a grid block average. We use overbars to indicate a spatial average over the x_1, x_2 position variables, at fixed x_3. Thus $\overline{f_1}$ is the volume fraction averaged over all x_1, x_2 and one mesh block in the x_3 direction. The concentration fluctuation, $\sigma(x_3)$, defined through the variance

$$\sigma^2 = \overline{(f_1 - \overline{f_1})^2}(x_3) \ , \tag{4.2}$$

is the standard deviation of the volume fraction $f_1(x_3)$. It is a function of the x_3-direction height. The average molecular mixing fraction, $\theta(x_3)$, is defined as

$$\theta = \frac{\overline{f_1 f_2}}{\overline{f_1}\,\overline{f_2}} = \frac{\overline{f_1} - \overline{f_1^2}}{\overline{f_1} - \overline{f_1}^2} = 1 - \frac{\sigma^2}{\overline{f_1}\,\overline{f_2}} \ . \tag{4.3}$$

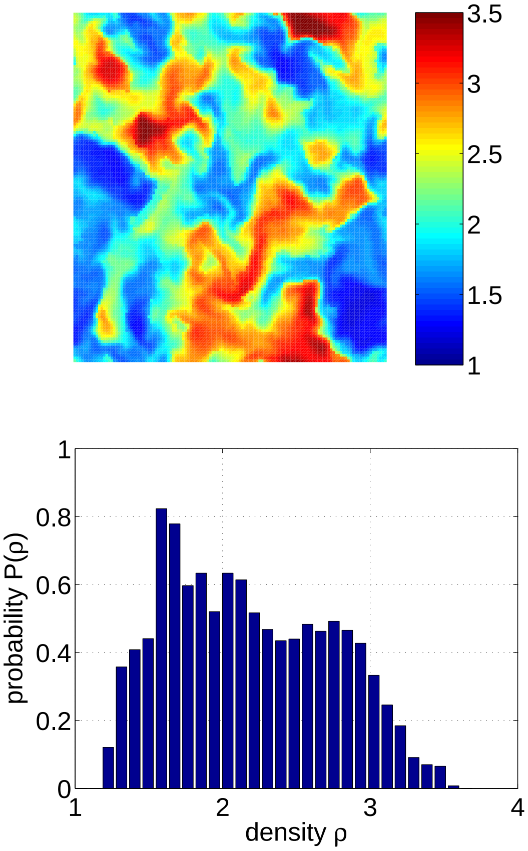

Figure 4.1: Density plot of a cross section through the middle of the mixing zone and the probability distribution fuction (pdf) for the simulation with mass diffusion at $t = 21$.

We can interpret the numerator and denominator in (4.3) in terms of chemical reactions between the two fluids. Assume a binary reaction. Then the numerator and denominator of (4.3) are proportional to the mean rate reaction and the perfectly stirred reaction rate. Thus θ is in this sense a measure of the amount of mixing that has occurred. Integrating the numerator and the denominator of $\theta(x_3)$, we define the molecular mixing fraction across the mixing zone as

$$\Theta = \frac{\int \overline{f_1 f_2}\, \mathrm{d}x_3}{\int \overline{f_1}\, \overline{f_2}\, \mathrm{d}x_3} \ . \tag{4.4}$$

For ideal or immiscible fluids (with surface tension and no physical mass diffusion), the above definitions of θ, Θ in terms of volume fractions are satisfactory. For the simulation of miscible fluids with physical mass diffusion, we need concentration variables in place of the volume fraction variables used above. For simplicity, we still denote these as f_1 and f_2.

By assuming that a stoichiometric mixture occurs for $f_1 = 1/2$, we define a different mixing parameter

$$\Xi = \frac{\int \overline{\min(f_1, f_2)}\, \mathrm{d}x_3}{\int \min(\overline{f_1}, \overline{f_2})\, \mathrm{d}x_3} \,. \tag{4.5}$$

The definition of the mixing parameter Ξ is the ratio of mean of the total reaction product to the totally stirred reaction product, for a reaction which proceeds to completion prior to any further diffusion (mixing) [8, 33]. Figure 4.1 shows the density cross section at the middle of the mixing zone and the corresponding probability distribution fuction (pdf) for the miscible case of simulation at late time. The pdf shows how much mixing occurs. As it mixes more, it follow more a normal distribution.

In Youngs' paper [33], with the density rate $\rho_1/\rho_2 = 3$, Θ increases as the mesh resolution $\xi = \delta x/(\alpha A g t^2)$ approaches zero. It is there determined that Θ is approximately 0.85 by extrapolating to $\xi = 0$. It is close to 0.7 in the experiments of Wilson and Andrews [32] with low Atwood number. Simulations by Dalziel *et al.* [9] and experiments by Linden *et al.* [21] yield similar values. In a high resolution LES study of Cabot [3], Ξ is nearly identical to Θ and increases and approaches 0.79 as time advances after a period of initial entrainment.

A more precise description of our method calculating the volume fraction f_1 is the following. Let $\rho_{\min}$ be the minimum value of ρ_1 and let $\rho_{\max}$ be the maximum value of ρ_2 at the interface at time $t = 0$. In a regular cell which is not cut by the interface, we find the component at the center of the cell. If the density is greater than the maximum density, we set it to the maximum density; if it is smaller than the minimum density we set it to the minimum density. The concentration for a regular cell is

$$\begin{aligned} f_1 &= \frac{\rho_{\max} - \rho}{\rho_{\max} - \rho_{\min}}, && (4.6) \\ f_2 &= 1 - f_1, && (4.7) \\ f_1 f_2 &= f_1 * (1 - f_1) && (4.8) \end{aligned}$$

where ρ is the density at the center. The inequality

$$\rho_{\min} \leq \rho \leq \rho_{\max} \ , \tag{4.9}$$

based on incompressible flow and properties of the diffusion equation, leads to

$$0 \leq f_1 \leq 1 \ . \tag{4.10}$$

For an irregular cell which is cut by the tracked interface, for instance, a corner case, we first identify the phase which the center point (A) belongs to and a corner point (B) which is in the other phase. See Figure 4.2.

The concentration is defined as

$$\begin{aligned} f_1 &= \frac{\rho_{\max} - \overline{\rho}}{\rho_{\max} - \rho_{\min}}, && (4.11) \\ f_2 &= 1 - f_1, && (4.12) \\ f_1 f_2 &= f_1 * (1 - f_1) && (4.13) \end{aligned}$$

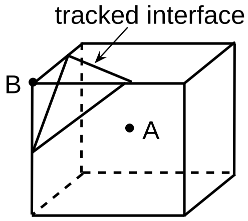

Figure 4.2: An irregular cell cut by the tracked interface (a corner case)

where

$$\overline{\rho} = \rho_A * V_A + \rho_B * V_B \tag{4.14}$$

where ρ_P is the density at the point P and V_P is obtained by measuring the volume (including the point) which is determined by the interface.

Measurements of miscible experiments and analysis of untracked (numerically mass diffusive) simulations also lead to concentrations rather than to volume fractions, so the above definitions are consistent with this usage.

In a high resolution LES study of Cabot [3], Ξ is nearly identical to Θ and increases and approaches 0.79 as time advances after a period of initial entrainment.

Next we examine the influence of the averaging length scale. For multiple cell averages, we add the one cell averaged f_1's and divide this sum by the number of cells. f_1 and $f_1 f_2$ are silmilarly averaged. Based on these $f_1, f_2, f_1 f_2$ we define the average molecular mixing fraction θ for the miscible case. We consider block averaged volume fractions, with an averaging block size $n\Delta x_1 \times n\Delta x_2 \times n\Delta x_3$, that is an average over n^3 cells. Thus the domain is divided by blocks. To obtain the layer averaged volume fraction in this case, the sum of the block-averaged volume fractions from one block

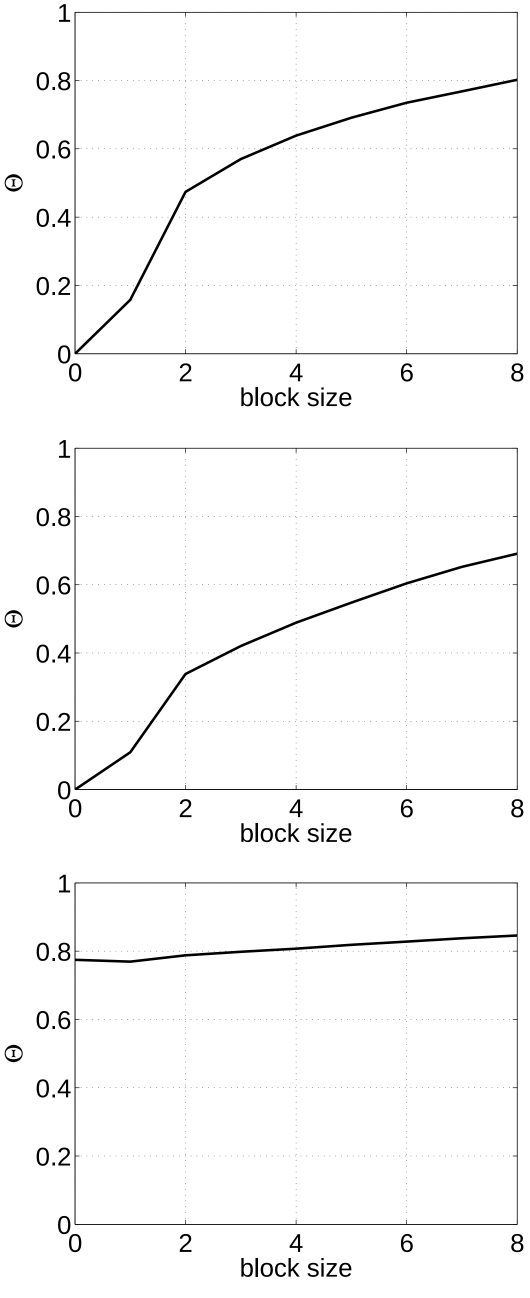

Figure 4.3: The molecular mixing fraction Θ *vs.* the block grid size, expressed as a multiple of Δx. Ideal case at $t = 15$ (top), immiscible case at $t = 14$ (middle), miscible case at $t = 15$ (bottom).

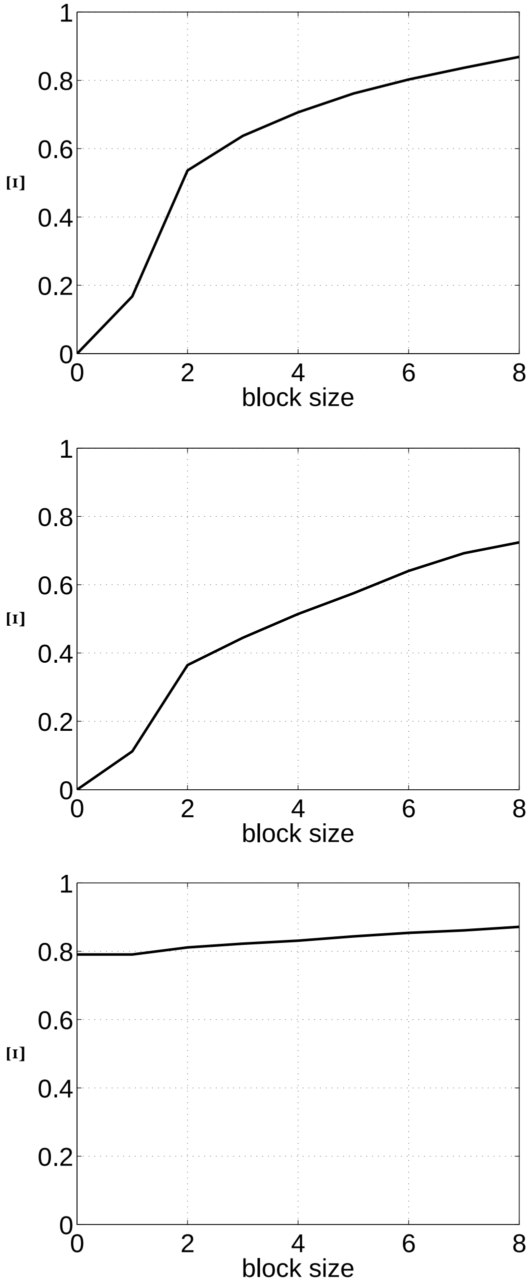

Figure 4.4: The mixing parameter Ξ *vs.* the subgrid size. Ideal case at $t = 15$ (top), immiscible case at $t = 14$ (middle), miscible case at $t = 15$ (bottom).

layer is normalized by the number of blocks per layer, which is the total number of grid blocks divided by n^2. The previously introduced quantities in this section can be recalculated based on this block-averaged volume fraction instead of f_1.

In Figure 4.3, we present Θ *vs.* the block size for the three simulations (ideal, surface tension and mass diffusion). The mixing values $\Theta = 0$ and $\Xi = 0$ for zero block size averaging (no averaging) for the ideal and immiscible fluids are guaranteed from considerations of microscopic physics. The unaveraged nonzero value 0.8 at zero block size for the miscible fluids results from physical mass diffusion, in agreement with experimental values. Figure 4.4 shows a similar plot for Ξ which is generally slightly bigger than Θ but those are nearly identical, which is also reported in the previous work done by Cabot [3]. For the ideal and surface tension simulations, a block averaging size $(4\Delta x)^3$ to $(8\Delta x)^3$ generates a $\Theta \sim 0.6 - 0.8$, which is similar to that found in previous works. For the ideal and immiscible simulations, we conclude that fluid entrainment at these length scales produces average (but not extreme) results comparable to numerical mass diffusion in untracked codes. For the physically mass diffusive simulations, we see little need for a mass diffusion subgrid model from the present analysis.

The approximate agreement of the unaveraged mixing parameter Θ for the mass diffusion simulation, comparing tracked and untracked simulations and experiments is perhaps surprising. We have observed significant differences among our data, experiments and untracked numerically mass diffusive simulations in regard to numerical mass diffusion. These differences are recorded in the mixing rate α_{ren} and the time dependent Atwood number $A(t)$, previously defined in this section. While α_{ren}, $A(t)$ and Θ are measures of mixing, they are not the same measure. α_{ren} and $A(t)$ are sensitive to extreme values while Θ is sensitive to average values. To visualize the differences between these two measures of mixing more clearly, we display in Figure 4.5

the evolution of density in a plane through the middle of the bubble region, for the mass diffusion simulation at times $t = 7, 15, 21$. The smaller bubbles, on the verge of extinction, are also more highly diffused, and contribute to the high mixing rate in Θ, while the larger bubbles, to feed continued overall RT mixing rate growth (*i.e.* α_{ren}), show a high density contrast. In this sense, θ shows the high degree of average mixing, while α_{ren} and $A(t)$ show only a moderate degree of mixing of extreme values.

In Fig. 4.6 we examine the average molecular mixing fraction θ as a function of x_3 at times $t = 7, 15, 21$. The molecular mixing fraction θ displays a uniformly high degree of average mixing.

4.2 Spectral Analysis

Power spectra are calculated by performing a 2D Fast Fourier Transformation (FFT) on data defined on a horizontal plane, for example the mid-plane (the position of the initial interface) and taking the magnitude of the Fourier transformed data. The 2D Discrete Fourier Transform (DFT) for data $f(j_1, j_2)$ centered at cell j_1, j_2, of size $N \times N$ is calculated by

$$\hat{f}(k_1, k_2) = \frac{1}{N^2} \sum_{j_1=0}^{N-1} \sum_{j_2=0}^{N-1} f(j_1, j_2) \exp(-2\pi i k_1 j_1 / N) \exp(-2\pi i k_2 j_2 / N) \ , \qquad (4.15)$$

where k_1 and k_2 are the x_1 and x_2 directional wave mode numbers, which satisfy $0 \leq k_1, k_2 \leq N - 1$. For the case of an irregular cell with fractional volumes in each fluid, the fluctuation is cell averaged with a block size 1 as was done in the previous section to define $f(j_1, j_2)$. The scalar wave number k is calculated by $k = \sqrt{k_1^2 + k_2^2}$. The power spectrum is averaged over k values in an interval $(k - 1/2, k + 1/2)$ to reduce noise. We use the Matlab $2D$ Fast Fourier Transformation. A simple example code is given below.

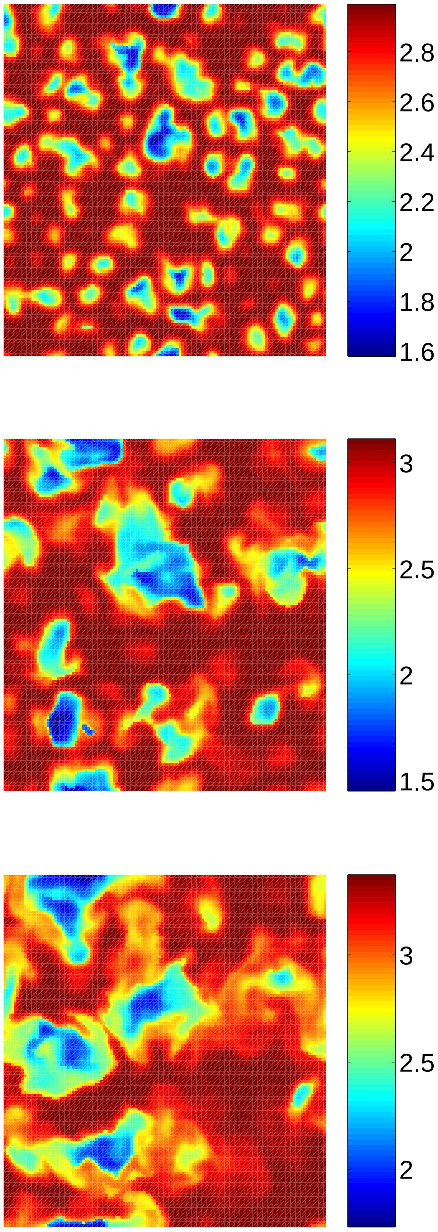

Figure 4.5: Density plot of a cross section through the middle of the bubble region, for the mass diffusion simulation, at $t = 7, 15, 21$. Color plot available online.

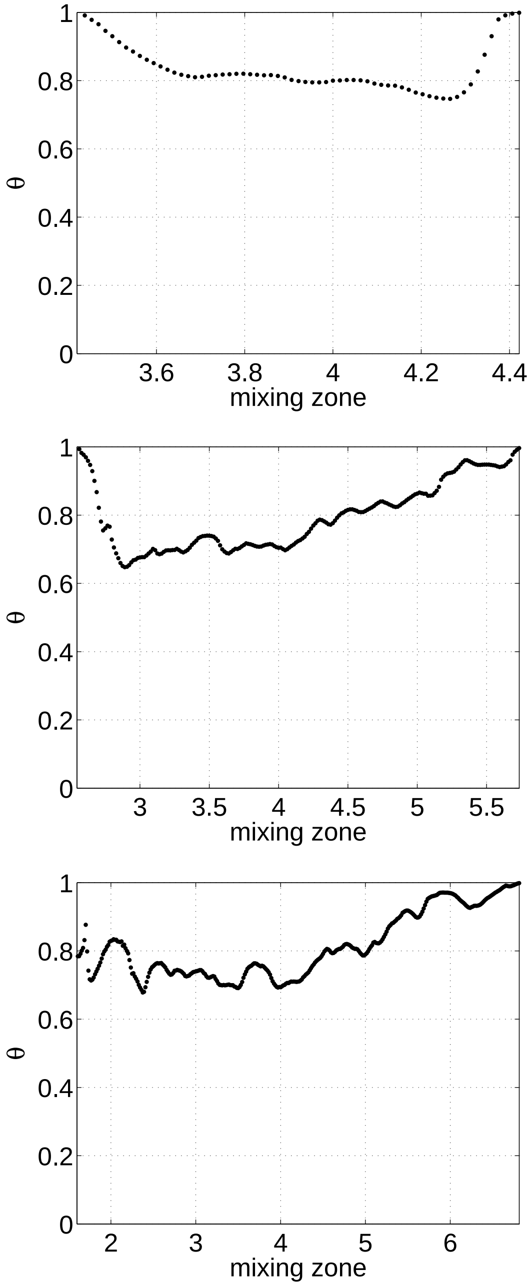

Figure 4.6: The mixing parameter θ *vs.* the mixing zone height for the mass diffusion simulation at $t = 7, 15, 21$.

```
V = load('velocity');

% V is N x N velocity over the mid-plane.

VF = load('volume_fraction');

% VF is N x N volume fraction overthe mid-plane.

Vfluc = (V - mean(mean(V)).*ones(N,N)).^2.*VF;

% Vfluc is fluctuation of the velocity which isthe varience of V.

Vspec = abs(fft2(Vfluc)./N^2);

% Vspec is the N x N spectrum of Vfluc calculated

% from Fourier transform of Vfluc.
```

Then the calculated spectrum can be plotted by using the following code.

```
if mod(N,2) == 0

ind_end = N/2; % Nyquist wave number

else

ind_end = (N+1)/2;

end

I = ind_end^2;

wave_number = zeros(I,1);

annulusVspec = zeros(I,1);

% This is the averaged spectrum in annulus.

ct = 1;

for i = 1:ind_end

for j = 1:ind_end

if((sqrt((i-1)^2+(j-1)^2)) < (ind_end-0.5))

wave_num(ct) = sqrt((i-1)^2+(j-1)^2);

VSPEC(ct) = Vspec(i,j);
```

```
ct = ct + 1;

end

end

end

[wn,ind] = sort(wave_num);

for k=1:I

spec_v(k) = VSPEC(ind(k));

end

wn_end = round(wn(I));

spec_avg_v = zeros(wn_end,1);

for m = 1:wn_end

count = 0;

for k = 1:I

if (wn(k) < (m+1/2)) & (wn(k) >= (m-1/2))

spec_avg_v(m) = spec_avg_v(m) + spec_v(k);

count = count+1;

end

end

spec_avg_v(m) = spec_avg_v(m)/count;

end

plot(1:wn_end,spec_avg_z(1:wn_end));

xlabel('wavenumber k');

ylabel('vertical velocity fluctuation');
```

where the initialization part has been omitted from the text code written above. This code is based on the Nyquist-Shannon sampling theorem stating that an analog signal waveform can be uniquely reconstructed, without error, from its samples if the signal is band-limited and the sampling frequency is greater than twice the signal bandwidth.

We present power spectra of the vertical velocity, density and kinetic energy fluctuations, and compare our results with the slope $-5/3$ based on the Kolmogorov law

$$E(k) \sim k^{-5/3} \ . \tag{4.16}$$

The region which follows the Kolmogorov law is the inertial subrange where energy is transfered to successively smaller scales.

We first examine the dependence of the power spectrum on height, x_3, in the mixing zone. Figure 4.7 shows power spectra of vertical velocity, density fluctuation and kinetic energy for the mass diffusion case at $t = 21$. These and other spectral plots are cut off at the Nyquist wave number $k = N/2$. At both mixing zone edges the spectra are small compared to those within the interior of the mixing zone. We take the spectrum from the mid-plane, which is also conventional, for our spectral analysis. Spectrum averaged over the whole mixing zone also gives a similar result. Both ways are used in other studies.

Figure 4.8 shows the spectra for the vertical velocity, density fluctuation and kinetic energy fluctuations for the mass diffusion simulation, calculated on the mid-plane, for three different times. This figure shows that the energy containing region decreases while the inertial range expands as time advances. Also we can see the dissipation region following the inertial range. In each figure, we locate a straight line with the Kolmogorov slope $-5/3$ as a reference. The figure shows a near match to this slope. Previous works [3, 9, 33, 34] report a Kolmogorov velocity spectrum or one close to it, but generally do not distinguish between alternate theories for

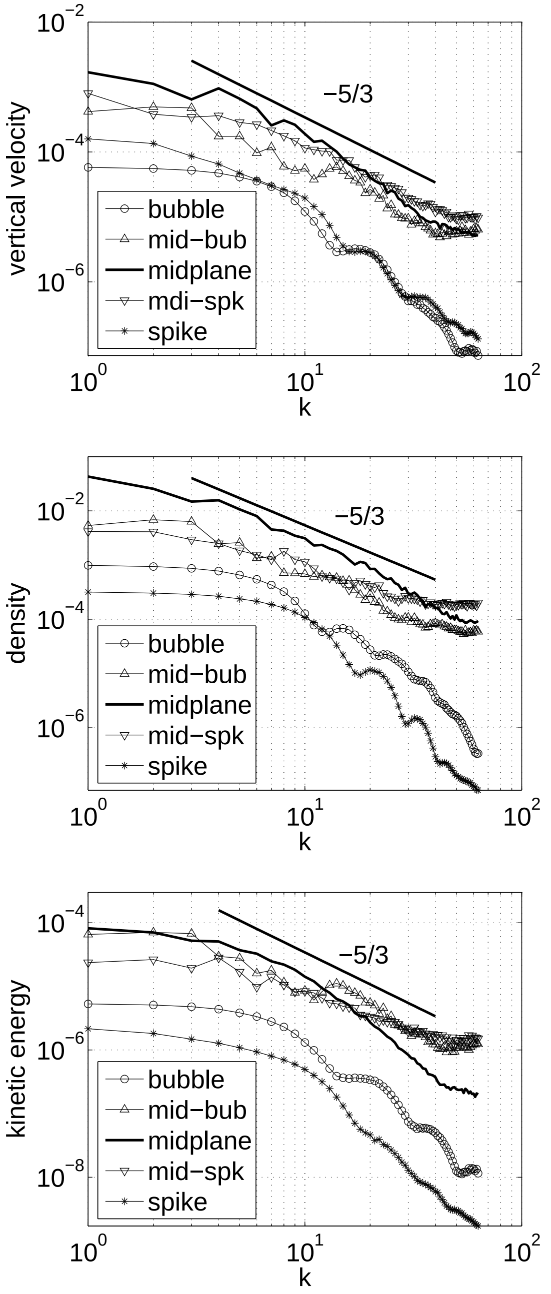

Figure 4.7: Power spectra of vertical velocity, density, and kinetic energy fluctuations (presented top to bottom) for the mass diffusion simulation at t = 21, taken at five different horizontal planes through the mixing zone.

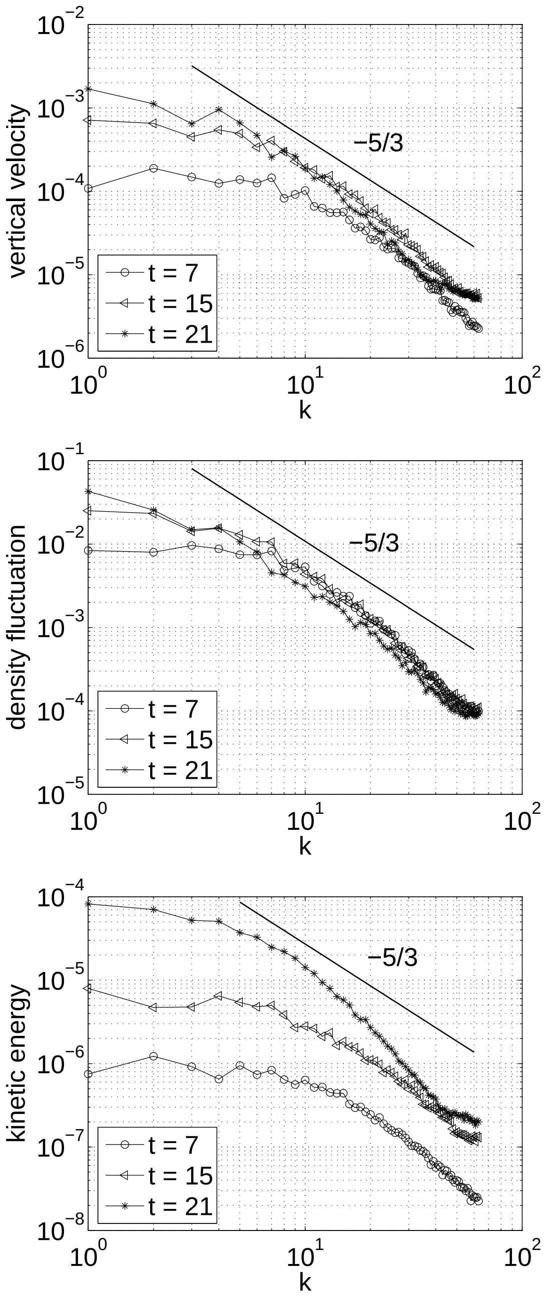

Figure 4.8: Power spectra of vertical velocity, density, and kinetic energy fluctuations (presented top to bottom) from the mid-plane for the mass diffusion simulation at $t = 7, 15, 21$.

the scaling exponent [8]. Cabot [3] reports a smaller than Kolmogorov slope for the density fluctuations. Poujade [26] argues theoretically that the low wave number end of the self similar regime has a non-Kolmogorov behavior. There is a recent opinion concerning the slope of this region [26], which states that the slope right after the wave number corresponding to the peak of the velocity spectrum is approximately -2 and that of concentration spectrum is around -1 and these slopes are maintained until right before the concentration dissipation. Our data does not clearly distinguish behavior -2 and $-5/3$, but it does not suspect the slope -2 for the concentration.

Each plot in Figure 4.8 show a characteristic upturn for k values in the range $45 \sim 60$, especially at late time, corresponding approximately to the lengths $2\Delta x$ to $3\Delta x$. In this range, the fluctuations are accumulating. They cannot be passed on to smaller grid levels as these are not available in the computation. The normal design of a subgrid algorithm will remove this buildup through dissipation, so that the power law spectrum will continue with its trend to these largest available k values. We can see these upturns in all the plots for density, velocity, and kinetic energy, which indicates the need for a subgrid model in the mass (continuity) equation and the momentum equation.

4.3 Subgrid Model

The basic theory, derivations and notations for subgrid model presented here are given in the book by Pope [25]. A filtering operation is defined to decompose a field $U(\mathrm{x}, \mathrm{t})$ into the sum of a filtered (or resolved) component u and a residual (or subgrid scale) component u'. In Chapter 3, we introduced our averaged phase quantities which are averaged in a cell. Since these quantities are filtered though a given grid we need a subgrid model to find the residual components. This brings the need for residual terms in the mass, momentum and energy equations so that these terms can be added to the resolved transport terms. Here we consider the mass and momentum equations only in this dissertation. Whether we need these terms or not can be determined by calculating the value of those terms and comparing them with the corresponding original physical quantities. We recall that ν denotes the diffusivity in the mass equation and μ does the viscosity in the momentum equation in Chapter 3.

We introduce subgrid models for mass and momentum equations. The mass and momentum equations without heat conductivity are

$$\begin{aligned} \frac{\partial \rho}{\partial t} + \frac{\partial \rho v_i}{\partial x_i} &= \nu \frac{\partial^2 \rho}{\partial {x_i}^2} && (4.17) \\ \frac{\partial v_j}{\partial t} + \frac{\partial v_i v_j}{\partial x_i} &= \mu \frac{\partial^2 v_j}{\partial {x_i}^2} - \frac{1}{\rho}\frac{\partial p}{\partial x_j} \ . && (4.18) \end{aligned}$$

Considering that

$$\begin{aligned} \overline{\rho v_i} &\neq \overline{\rho}\, \overline{v_i} \ , && (4.19) \\ \overline{v_i v_j} &\neq \overline{v_i}\, \overline{v_j} \ , && (4.20) \end{aligned}$$

filtering of the equations (4.17) yields

$$\begin{aligned} \frac{\partial \overline{\rho}}{\partial t} + \frac{\partial \overline{\rho}\, \overline{v_i}}{\partial x_i} &= \nu \frac{\partial^2 \overline{\rho}}{\partial x_i^2} - \frac{\partial(\overline{\rho v_i} - \overline{\rho}\, \overline{v_i})}{\partial x_i} \ , && (4.21) \\ \frac{\partial \overline{v_j}}{\partial t} + \frac{\partial \overline{v_i}\, \overline{v_j}}{\partial x_i} &= \mu \frac{\partial^2 \overline{v_j}}{\partial x_i^2} - \frac{\partial(\overline{v_i v_j} - \overline{v_i}\, \overline{v_j})}{\partial x_i} - \frac{1}{\rho}\frac{\partial \overline{p}}{\partial x_j} \ . && (4.22) \end{aligned}$$

Let $q_i = \overline{\rho v_i} - \overline{\rho}\, \overline{v_i}$ and $\tau_{ij} = \overline{v_i v_j} - \overline{v_i}\, \overline{v_j}$. The subgrid scalar stress $\mathbf{q}$ and the subgrid stress tensor τ show the influence of the subgrid scales on the resolved ones.

A simple model for these subgrid flux terms is

$$
\begin{aligned}
q_i &= \nu_{SGS} \frac{\partial \rho}{\partial x_i} \ , && (4.23) \\
\tau_{ij}^r &= \tau_{ij} - \frac{2}{3}\kappa_r \delta_{ij} = -\mu_{SGS} \left(\frac{\partial \overline{u_i}}{\partial x_j} + \frac{\partial \overline{u_j}}{\partial x_i} \right) \ , && (4.24)
\end{aligned}
$$

where $\kappa_r = \frac{1}{2}\tau_{ij}$ is the residual kinetic energy. The kinetic energy term will be included in pressure term which is the last term in the equation (4.22). Thus the residual subgrid stress tensor is traceless. The two equations (4.21) and (4.22) eventually become

$$
\begin{aligned}
\frac{\partial \overline{\rho}}{\partial t} + \frac{\partial \overline{\rho}\ \overline{v_i}}{\partial x_i} &= (\nu + \nu_{SGS}) \frac{\partial^2 \overline{\rho}}{\partial x_i^2} \ , && (4.25) \\
\frac{\partial \overline{v_j}}{\partial t} + \frac{\partial \overline{v_i}\ \overline{v_j}}{\partial x_i} &= (\mu + \mu_{SGS}) \frac{\partial^2 \overline{v_j}}{\partial x_i^2} - \frac{1}{\rho}\frac{\partial \overline{p}}{\partial x_j} \ . && (4.26)
\end{aligned}
$$

To determine the need for these subgrid models we estimate the magnitude of the subgrid mass diffusion ν_{SGS} and the subgrid viscosity μ_{SGS}. Pullin [27] proposed a subgrid model for the flux of a passive scalar within the framework of the stretched vortex subgrid stress model. We do not have this vortex based subgrid model implemented for our simulation at this moment. As a temporary substituete, we adopt a hypothesis that the subgrid Schmidt number is 1 so that we can use the subgrid viscosity to calculate the subgrid diffusivity for the miscible simulation.

To calculate the subgrid viscosity we use the simplest subgrid model, of Smagorinsky type, which relates the eddy viscosity to the large-scale strain tensor. The strain tensor is defined as

$$
\overline{S}_{ij} = \frac{1}{2} \left(\frac{\partial \overline{u_i}}{\partial x_j} + \frac{\partial \overline{u_j}}{\partial x_i} \right) \ , \qquad (4.27)
$$

and

$$\overline{S} = \sqrt{2\overline{S_{ij}}\ \overline{S_{ij}}}\ . \tag{4.28}$$

The tensor τ_{ij}^{r} can be modeled by

$$\tau_{ij}^{r} = -2\nu_r \overline{S_{ij}} \tag{4.29}$$

and mixing-length hypothesis gives

$$\nu_r = (C_s \triangle x)^2 \overline{S} \ \cong \ (C_s \triangle x)^2 \overline{S}\ . \tag{4.30}$$

For comparison to the physical mass diffusivity, expressed dimensionlessly in (2.4), we define a dimensionless subgrid diffusivity

$$\widetilde{\nu_{SGS}} = \frac{\nu_{SGS}}{\lambda\sqrt{Ag\lambda}}\ , \tag{4.31}$$

$$\nu_{SGS} = c^2 \Delta x^2 ||S||_2\ . \tag{4.32}$$

We present in Table 4.3 the planar averages of ν_{SGS}, ν and the ratio of them so that we can compare the magnitude of each values over the mixing zone. From this table we expect that the subgrid mass diffusion model is negligible since it is less than 1% of the physical mass diffusion. The extreme values for these subgrid quantities are not greatly larger than their mean values, see Figure 4.9. Neither the average nor the extreme values suggest a significant role for a subgrid mass diffusion model for this simulation.

	ν_{SGS}	ν	ν_{SGS}/ν
Bubble Tip	2.2 e-06	0.0054	0.0004
Mid Bubble	1.6 e-05	0.0054	0.003
Mid-plane	2.3 e-05	0.0054	0.004
Mid Spike	2.2 e-05	0.0054	0.004
Spike Tip	2.3 e-06	0.0054	0.0004

Table 4.1: Subgrid mass diffusion coefficients, averaged over horizontal planes, as computed by a Smagorinsky model, for $t = 21$ in the mass diffusion simulation data.

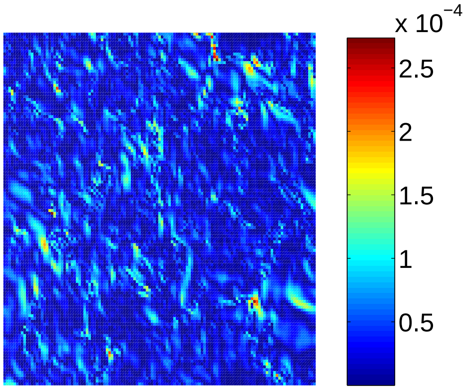

Figure 4.9: The mid-plane plot for ν_{SGS}, at $t = 21$ for the mass diffusion data. (Color available online.)

Chapter 5

Conclusion

We deal with two of somewhat separate issues in this thesis, a closure model and a study of turbulence in the RT data set.

The closures for v^*, p^* and $(pv)^*$ satisfy all required constraints of boundary conditions and conservation. The boundary constraints are given in (3.43). Phase k mass and total momentum are conserved in the absence of diffusion and viscosity in equation (3.34) and (3.35). Total energy is conserved according to equation (3.36). Entropy should not be conserved because averaging is non-adiabatic, but an entropy inequality is enforced [20].

Each closure has a very simple form for its coefficient d_k^q $(q = v,\ p,\ (pv))$ in Table 5. The closure model for v^*, p^*, $(pv)^*$ gives very good approximation to the exact expression with DNS data, within about 10% of the error while the model of Saurel et al. has about 30% of the overall error.

The insensitivity of our model is also verified, for which the inequality (3.50) can be a criteria. Here we note that this insensitivity for p^*, $(pv)^*$ is obtained by forcing the coefficient d_k^q to be positive. Table 5.2 summarize the sensitivity of our closure model to the choice of the coefficients d_k^q and to v^*, also the sensitivity of Saurel's model to the relaxation terms. The summary results of this table can be interpreted

	RT
d_1^v	(3.52)
d_1^p	1.0
d_1^{pv}	1.0

Table 5.1: Summary of d_k^q parameter choices for RT mixing. All choices except that for d_k^v in the RT case are insensitive.

	v^*	p^*	$(pv)^*$
RT: Closure sensitive to d_k^q ((3.50) or (3.83) invalid)	yes	no	no
RT: Closure sensitive to v^*	–	–	yes
RT: Relaxation important	no	late time	late time

Table 5.2: Summary properties related to the closures q^*. It is remarkable that the closures depend sensitively on their defining parameter d_k only in the case of the RT data for the v^* closure.

as follows. The sensitive case for (3.50) occurs for v^* closure only. This is because the computational frame is almost same as that of the average interface position. But as we see in Figure 3.10, the pressure tends to be equilibrated so that Δp is small while the averaged pressure is relatively big, which made the inequality (3.50) hold so that the closure for p^* is not sensitive to the choice of d^p. For $(pv)^*$, we find $(pv)^* \approx p^*v^*$ and the coefficient is included in p^* term so that the closure depends on v^* but the insensitivity comes from p^*. That is why the error between the closure and the exact expression is comparable to that of v^* even though it is not sensitive to the choice of d^{pv}. Our closure is compared with another closure models including the relaxation terms proposed by Saurel et al. and their models have about 30% of error. The relaxation terms make the results worse especially at late time.

In the second part of analysis following a classical turbulence study, we observe the time dependent Atwood number $A(t)$ and renormalized bubble growth rate α_{ren},different types of mixing behaviors from the average molecular mixing fraction

θ. Briefly, the grid level averaged mixing properties (related to θ) are shared among experiments, tracked and untracked simulations, while the extreme values (representing unmixed portions of the two fluid mixture, related to $A(t)$ and α_{ren}) are more pronounced in the tracked simulations than in the untracked ones.

We perform the spectral analysis to the velocity, density and kinetic energy. The spectral analysis of energy gives us a good agreement with Kolmogorov $-5/3$ energy decay law. In the spectrum we see the typical up-turn at large wave numbers, which indicates the need of a subgrid model.

We introduce and derive a basic subgrid model to adjust the up-turn. To do this we use Smagorinsky type of subgrid model. We expect that the magnitude of the residual terms is small by considering the small size of the up-turn. With the hypothesis that our subgrid Schmidt number Sc_{SGS} is 1, we have the result that the subgrid mass diffusion is negligible.

Chapter 6

Future Work

In this chapter, on-going and future work is briefly presented.

We extend the turbulent flow analysis in Chapter 4 to another problem which is Richtmyer-Meshkov instability (RM) in cylindrical geometry. Richtmyer-Meshkov instability occurs when the interface between two fluids with different densities is impulsively accelerated by the passage of a shock.

The 2D RM simulations were verified by a mesh convergence study. We also deal with simulations with two phases which are Tin as an exterior heavy fluid and Lucite as an interior light fluid. These two phases are initially separated by a perturbed circular interface which can be expressed by sine waves and the shock is moving inward from outer circular boundary. The initial Cartesian coordinates are transformed to a polar coordinates for the data analysis.

In this work, the dependence of the interfacial length on the computational mesh size and viscosity is observed. We also perform spectral analysis and the effect of Schmidt number (Sc) on the energy spectrum. It is known that the energy spectrum decays faster in the dissipation region as the Schmidt number is smaller. However, it might not be seen in our simulations in case that the resolved scale cutoff lies somewhere in the inertial range which result in showing independence of Sc. To see the effect of Sc, the implementation of the stretched-vortex subgrid model might be needed, which was proposed by Pullin et al. [27]

Bibliography

[1] A. Banerjee and M. J. Andrews. Statistically steady measurements of Rayleigh-Taylor mixing in a gas channel. *Physics of fluids*, 18(3):35107–1–35107–13, 2006.

[2] R. Bird, W. Stewart, and E. Lightfoot. *Transport Phenomena Second Edition.* John Wiley & Sons, New York, 2002.

[3] W. Cabot. Comparison of two- and three-dimensional simulations of miscible Rayleigh-Taylor instability. *Phys. Fluids*, 18(045101), 2006.

[4] Y. Chen. *Two Phase Flow Analysis of Turbulent Mixing in the Rayleigh-Taylor Instability.* PhD thesis, University at Stony Brook, 1995.

[5] Y. Chen, J. Glimm, D. H. Sharp, and Q. Zhang. A two-phase flow model of the Rayleigh-Taylor mixing zone. *Phys. Fluids*, 8(3):816–825, 1996.

[6] B. Cheng, J. Glimm, D. H. Sharp, and Y. Yu. A multiphase flow model for the unstable mixing of layered incompressible materials. *Phys. of Fluids*, 17:087102–1–07102–8, 2005. Paper No. 087102. LANL Preprint Number LA-UR-05-0078. Stony Brook University Preprint Number SUNYSB-AMS-05-01.

[7] A. Chinnayya, E. Daniel, and R. Saurel. Modelling detonation waves in heterogeneous energetic materials. *J. Comp. Phys.*, 196:490–538, 2004.

[8] A. W. Cook and Y. Zho. Energy transfer in Rayleigh-Taylor instability. *Phys. Rev. E.*, 66(026312), 2002.

[9] S. B. Dalziel, P. F. Linden, and D. L. Youngs. Self-similarity and internal structure of turbulence induced by Rayleigh-Taylor instability. *J. Fluid Mech.*, 399:1–48, 1999.

[10] D. Drew and S. Passman. *Theory of Multicomponent Fluids.* Applied Mathematical Sciences. Springer-Verlag, New York, 1999.

[11] D. A. Drew. Mathematical modeling of two-phase flow. *Ann. Rev. Fluid Mech.*, 15:261–291, 1983.

[12] Jian Du, Brian Fix, James Glimm, Xicheng Jia, Xiaolin Li, Yunhua Li, and Lingling Wu. A simple package for front tracking. *J. Comp. Phys.*, 213:613–628, 2006. Stony Brook University preprint SUNYSB-AMS-05-02.

[13] P. Flohr and J. C. Vassilicos. A scalar subgrid model with flow structure for large- eddy simulatins of scalar variances. *J. Fluid Mech.*, 407:315–349, 2000.

[14] E. George and J. Glimm. Self similarity of Rayleigh-Taylor mixing rates. *Phys. Fluids*, 17:054101–1–054101–13, 2005. Stony Brook University Preprint number SUNYSB-AMS-04-05.

[15] E. George, J. Glimm, X. L. Li, Y. H. Li, and X. F. Liu. The influence of scale-breaking phenomena on turbulent mixing rates. *Phys. Rev. E*, 73:016304–1–016304–5, 2006.

[16] J. Glimm and H. Jin. An asymptotic analysis of two-phase fluid mixing. *Bol. Soc. Bras. Mat.*, 32:213–236, 2001.

[17] J. Glimm, D. Saltz, and D. H. Sharp. Renormalization group solution of two-phase flow equations for Rayleigh-Taylor mixing. *Phys. Lett. A*, 222:171–176, 1996.

[18] J. Glimm, D. Saltz, and D. H. Sharp. Two-pressure two-phase flow. In G.-Q. Chen, Y. Li, and X. Zhu, editors, *Nonlinear Partial Differential Equations*, pages 124–148. World Scientific, Singapore, 1998.

[19] J. Glimm, D. Saltz, and D. H. Sharp. Two-phase modeling of a fluid mixing layer. *J. Fluid Mech.*, 378:119–143, 1999.

[20] H. Jin, J. Glimm, and D. H. Sharp. Entropy of averaging for compressible two-pressure two-phase models. *Phys. Lett. A*, 360:114–121, 2006. Stony Brook University Preprint number SUNYSB-AMS-06-08 and Los Alamos National Laboratory.

[21] P. F. Linden, J. M. Redondo, and D. L. Youngs. Molecular mixing in Rayleigh-Taylor instability. *J. Fluid Mech.*, 265:97–124, 1994.

[22] X. F. Liu, E. George, W. Bo, and J. Glimm. Turbulent mixing with physical mass diffusion. *Phys. Rev. E*, 73:056301–1–056301–8, 2006.

[23] X. F. Liu, Y. H. Li, J. Glimm, and X. L. Li. A front tracking algorithm for limited mass diffusion. *J. of Comp. Phys.*, 2007. Accepted. Stony Brook University preprint number SUNYSB-AMS-06-01.

[24] L. Malvern. *Introduction to the Mechanics of Continuous Medium.* Prentice Hall, 1969.

[25] Stephen B. Pope. *Turbulent Flows.* Cambridge University Press, 2000.

[26] O. Poujade. Rayleigh-Taylor turbulence is nothing like kolmogorov's in the self similar regime. *Phys. Rev. Lett.*, 97(18):185002–1–185002–4, 2006.

[27] D. Pullin. A vortex pased model for the subgrid flux of a passive scalar. *Phys. of Fluids*, 12:2311–2319, 2000.

[28] K. I. Read. Experimental investigation of turbulent mixing by Rayleigh-Taylor instability. *Physica D*, 12:45–58, 1984.

[29] R. Saurel and R. Abgrall. A multiphase Godunov method for compressible multifluid and multiphase flows. *J. Comput. Phys.*, 150:425–467, 1999.

[30] V. S. Smeeton and D. L. Youngs. Experimental investigation of turbulent mixing by Rayleigh-Taylor instability (part 3). AWE Report Number 0 35/87, 1987.

[31] Forman Williams. *Combustion Theory.* Addison-Wesley Co., Reading, 1965.

[32] P. Wilson and M. Andrews. Spectral measurements of Rayleigh-Taylor mixing at small atwood number. *Physics of Fluids*, 14(3):938–945, 2002.

[33] D. L. Youngs. Three-dimensional numerical simulation of turbulent mixing by Rayleigh-Taylor instability. *Phys. Fluids A*, 3:1312–1319, 1991.

[34] D. L. Youngs. Application of miles to Rayleigh-Taylor and Richtmyer-Meshkov mixing. Technical report, 2003. Technical Report 4102, 16th AIAA Computational Fluid Dynamics Conference.